47th AIAA/ASME/SAE/ASEE Joint Propulsion Conference & Exhibit
31 July - 03 August 2011, San Diego, California

AIAA 2011-6029

Transverse Waves in Simulated Liquid Rocket Engines

Charles T. Haddad* and Joseph Majdalani†
University of Tennessee Space Institute, Tullahoma, TN 37388

This work introduces a closed-form analytical solution for the transverse vorticoacoustic wave in a circular cylinder with headwall injection. This particular configuration mimics the conditions leading to the onset of traveling radial and tangential waves in a simple liquid rocket engine (LRE). In order to model the showerhead into a simulated LRE thrust chamber, two injection profiles are considered: a top-hat, uniform flow and a bell-shaped, sinusoidal profile that satisfies the no-slip physical requirement along the circumference of the injector faceplate. Assuming a short cylindrical chamber with an injecting headwall, regular perturbations are used to linearize the problem's mass, momentum, energy, ideal gas, and isentropic relations. A Helmholtz decomposition is subsequently applied to the first-order disturbance equations, thus giving rise to a compressible, inviscid, acoustic set that is responsible for driving the unsteady motion, and to an incompressible, viscous, vortical set that is driven by virtue of coupling with the acoustic mode along solid boundaries. While the acoustic mode is readily recovered from the wave equation entailed in this analysis, the induced vortical mode is resolved using boundary layer theory and a judicious expansion of the rotational set with respect to a small viscous parameter, δ. After some effort, an explicit formulation is arrived at for each of the uniform and bell-shaped injection profiles. The two solutions are then presented and compared at fixed spatial locations within the chamber. The penetration depth of the unsteady boundary layer is also characterized. Unlike the solution based on uniform headwall injection (that permits slip at the sidewall), the vorticoacoustic wave based on the bell-shaped mean flow is found to be more realistic, being capable of securing the no-slip requirement at both headwall and sidewall boundaries. It may hence be viewed as an improved physical representation of the transverse wave motion in a circular enclosure that idealizes the unsteady flowfield in a simulated liquid rocket engine.

Nomenclature

a_0	=	speed of sound of incoming flow, $(\gamma RT_0)^{1/2}$
$\boldsymbol{e}_r, \boldsymbol{e}_\theta, \boldsymbol{e}_z$	=	unit vectors in $r, \theta,$ and z directions
L	=	chamber length
M_b	=	average blowing/burning Mach number at headwall
OF	=	overshoot factor
p	=	pressure
Pr	=	Prandtl number, ratio of kinematic viscosity to thermal diffusivity
r, θ, z	=	radial, tangential, and axial coordinates
R	=	chamber radius
Re_a	=	acoustic Reynolds number, $(a_0 R)/\nu_0$
Re_b	=	blowing Reynolds number at the headwall, $(U_b R)/\nu_0$
S	=	Strouhal number, $K_{mn}/M_b = (\omega_0 R)/U_b$
S_p	=	effective penetration number
t	=	time
T	=	temperature

*Graduate Research Assistant, Mechanical, Aerospace and Biomedical Engineering Department. Member ASME.
†H. H. Arnold Chair of Excellence in Advanced Propulsion, Mechanical, Aerospace and Biomedical Engineering Department. Associate Fellow AIAA. Fellow ASME.

$\boldsymbol{u}$ = total velocity vector
$U_b(r)$ = blowing velocity profile at the headwall
$\boldsymbol{U}$ = mean flow velocity vector
V_w = propagation velocity of vortical waves in the axial direction
y_p, z_p = penetration depth of rotational elements in the y and z directions, respectively
z_{OS} = locus of unsteady velocity overshoot

Greek
δ = viscous parameter, $\sqrt{1/Re_a}$
δ_d = dilatational parameter, $\delta\sqrt{\eta_0/\mu_0 + 4/3}$
ε = wave amplitude
γ = ratio of specific heats
η = bulk viscosity
λ = spatial wave length
μ = dynamic viscosity
ν = kinematic viscosity, μ/ρ
ρ = density
$\boldsymbol{\omega}$ = unsteady vorticity
ω_0 = non-dimensional circular frequency
$\boldsymbol{\Omega}$ = mean vorticity

Subscripts
0 = mean chamber properties

Superscripts
* = dimensional variables
$'$ = unsteady flow variable
$\bar{}$ = steady flow variable

I. Introduction

COMBUSTION instability has long been recognized as one of the most challenging problems plaguing large scale combustors. In fact, it is considered as one of the chief obstacles in the development of liquid rocket engines. Combustion instability was observed as early as the late 1930s both in solid and liquid rocket engines. Numerous studies have been conducted to quantify its sources, and these include experimental,[1] numerical,[2] and analytical investigations.[3]

In liquid rocket engines, transverse combustion instabilities are identified by large pressure oscillations, in a plane perpendicular to the axis of the combustion chamber, and corresponding frequencies that closely match linear chamber acoustics.[4,5] Experimental observations have often suggested that the instabilities involve large amplitude oscillations with steep gradients in the direction of the flow. For instance, Clayton, Sotter and co-workers[6-8] investigated high amplitude tangential oscillations using a heavily instrumented, laboratory scale, 20 klbf thrust engine. They recorded steep-fronted pressure oscillations with peak-to-peak amplitudes that are one order of magnitude larger than the mean chamber pressure. Although the response rate of their pressure transducers was not small enough to accurately capture the resulting waves, their acquired data displayed large amplitude spikes followed by long and shallow pressure segments.

Along similar lines, numerical studies have focused on the characterization of the transverse waves and their effects on combustion instability for different rocket configurations. By way of example, Ando, Inaba and Yamamoto[9] simulated the generation of transverse waves in a pulse denotation engine and deduced that the strength of the blasts increased where transverse waves collided. Other researchers, such as Chandrasekhar and Chakravarthy,[10] deduced from their simulations that transverse waves could be induced by wall vibrations to the extent of producing longitudinal oscillations.

The earliest analytical studies of oscillatory waves in a ducted environment with injecting walls were undertaken by Hart and McClure,[11,12] Culick[13] and others.[14-18] Their models led to the few analytical formulations describing

the behavior of oscillatory flows inside porous walls. Other researchers applied asymptotic approaches to linearize the Navier-Stokes equations and deduce the predicted wave behavior. This effort was prompted by the long-standing belief that the presence of a tangential acoustic velocity can give rise to a traveling shear wave. In 1956, theoretical work by Maslen and Moore[19] hinted that tangential waves could not steepen as in the case of longitudinal waves. Their study on tangential wave development used a circular cylinder with zero mean flow. In 1962, Crocco, Harrje and Reardon[20] used small perturbations and separation of variables to predict the stability limit of liquid rocket engines. Their work showed that the stability of their rocket depended on the radial and tangential modes as well as the chamber's exit Mach number. Later studies[21] took into account the effects of the mean flow on wave growth and propagation in a cylinder with transpiring wall, this being the traditional geometry used to simulate a solid rocket motor.

Studies that followed emphasized the satisfaction of the no-slip boundary conditions and provided viscous and rotational corrections to the acoustic field in a solid rocket motor. On one hand, Brown, Dunlap and collaborators[22,23] provided experimental data that confirmed the behavior of the longitudinal oscillations in the chamber. Their results showed that the models available at the time failed to satisfy the fluid's behavior next to the wall. On the other hand, Vuillot and Avalon[24] studied the growth of the sidewall boundary layer. Their analytical results predicted a thick boundary layer at the sidewall, specifically one that extended over the entire chamber volume for specific Reynolds numbers. Later analytical pursuits relied on perturbation theory to provide closed-form solutions to the problem. Researchers discovered that the behavior of the oscillatory flow and its propagation into a rocket chamber depended heavily on the mean flow and injection patterns.[14,25-27] Using asymptotic techniques such as WKB, Majdalani and coworkers were able to identify the dependence of the rotational boundary layer region on the penetration number, a keystone parameter that combines the injection Reynolds and Strouhal numbers in a non-intuitive way (Re/S^2).

Since the behavior of the waves remains coupled with the mean flow, the proper selection of the latter stands at the forefront of a meaningful physical representation of the problem at hand. In fact, early analytical investigations of the combustion instability problem may have inadvertently started with Berman[28] who, despite his interest in an entirely different industrial application, provided the means to solve for the steady state flowfield in a cylinder with injecting sidewall. Later, Yuan and Finkelstein[29] produced asymptotic solutions for the large injection and suction cases. Several studies followed, and these have mostly focused on unraveling different mean flows in porous enclosures with a variety of injection configurations.

In hindsight, most of these studies seem to have primarily concentrated on the oscillatory motion within elongated solid rocket motors, and much fewer have tackled the liquid rocket engine case.[19,20,30] Recently, Fischbach, Flandro and Majdalani[18] considered the transverse wave propagation in such rockets, with the purpose of understanding the mechanism of acoustic streaming. Albeit a secondary objective of theirs, they also analyzed the growth of the vorticoacoustic boundary layer at the headwall. Their configuration is somewhat analogous to the solid rocket motor case, where the sidewall substitutes for the headwall of a LRE.

In the present investigation, we consider the oscillatory flowfield inside a cylinder of small aspect-ratio and injecting headwall. The mean fluid motion is induced by two injection profiles, either uniform or bell-shaped. In addition to the mean flow, the presence of small-amplitude oscillatory waves is accounted for. These self-excited waves give rise to a complex fluid structure that we wish to describe. Following the small perturbation approach introduced by Chu and Kovásznay,[31] the equations of motion are recast into two sets: one controlling the mean flow behavior, and the other describing the oscillatory motion. Then, using a Helmholtz decomposition, the first-order fluctuations are separated into a pair of acoustic and vortical fields. Presently, these techniques will be used to derive an improved asymptotic solution for the oscillatory motion in a circular chamber in general, and a simulated LRE in particular. Using a systematic application of boundary layer theory, an alternate mathematical formulation will be achieved and compared to previous work on the subject.[18] At the outset, the oscillatory flow approximation based on the bell-shaped injection pattern will be shown to provide an improved representation of the actual wave motion in a simulated thrust chamber.

II. Formulation

A. Geometry

As shown schematically in Fig. 1, the idealized thrust chamber is simulated as a circular cylinder that extends vertically from the center axis at $r^* = 0$ to the sidewall at $r^* = R$. Horizontally, the domain extends from $z^* = 0$ to L, where the headwall may be viewed as a porous surface across which flow may be injected at a velocity

$U_b(r)$. We also show in Fig. 1 the azimuthal coordinate, θ, and the transverse direction of unsteady velocity disturbances, u'_θ and u'_r, which denote the both tangential and radial oscillations. Given that this study is focused on a simulated LRE, the aspect ratio of the chamber under consideration is taken to be small, specifically less than or equal to unity, $L/R \le 1$.

B. Normalized System of Equations

It is helpful to first proceed by normalizing the flow variables according to

$$\begin{cases} p = p^* / P_0 & \boldsymbol{u} = \boldsymbol{u}^* / a_0 & r = r^* / R & T = T^* / T_0 \\ \rho = \rho^* / \rho_0 & t = t^* / (R / a_0) & z = z^* / R & \boldsymbol{\omega} = \boldsymbol{\omega}^* / (a_0 / R) \end{cases} \tag{1}$$

where reference properties are defined in the Nomenclature. The normalized governing equations for a viscous compressible fluid, with no body forces acting on it, may be expressed as

Mass:
$$\frac{\partial \rho}{\partial t} + \nabla \cdot (\rho \boldsymbol{u}) = 0 \tag{2}$$

Momentum:
$$\rho\left(\frac{\partial \boldsymbol{u}}{\partial t} + \boldsymbol{u} \cdot \nabla \boldsymbol{u} - \boldsymbol{u} \times \nabla \times \boldsymbol{u} \right) = -\frac{1}{\gamma} \nabla p - \delta^2 \nabla \times (\nabla \times \boldsymbol{u}) + \delta_d^2 \nabla (\nabla \cdot \boldsymbol{u}) \tag{3}$$

Energy:
$$\rho\left(\frac{\partial T}{\partial t} + \boldsymbol{u} \cdot \nabla T \right) = \frac{\gamma - 1}{\gamma} \left(\frac{\partial p}{\partial t} + \boldsymbol{u} \cdot \nabla p \right) + \frac{\delta^2}{Pr_0} \nabla^2 T \tag{4}$$

State:
$$p = \rho T \tag{5}$$

Isentropic relation:
$$p = \rho^\gamma \tag{6}$$

where Pr is the Prandl number, γ is the ratio of specific heats, and the viscous parameters δ and δ_d are given by

$$\delta = \sqrt{\frac{\nu_0}{a_0 R}} = \sqrt{\frac{1}{Re_a}}; \quad \delta_d = \delta \sqrt{\frac{\eta_0}{\mu_0} + \frac{4}{3}} \tag{7}$$

The bulk viscosity, also known as the dilatational viscosity η, is taken here at the reference conditions as η_0. It represents viscous shear associated with the volumetric-rate-of-strain, and is approximately set to zero when the fluid is incompressible according to the Stokes hypothesis.

C. Unsteady Disturbance Equations

As shown by Chu and Kovásznay,[31] the normalized flow variables can be decomposed in terms of a mean flow and an oscillatory component viz.

$$\boldsymbol{u} = M_b \boldsymbol{U} + \boldsymbol{u}'; \quad \boldsymbol{\omega} = \bar{\boldsymbol{\Omega}} + \boldsymbol{\omega}'; \quad p = 1 + p'; \quad \rho = 1 + \rho'; \quad T = 1 + T' \tag{8}$$

Substituting the instantaneous variables of Eq. (8) into Eqs. (2)–(6) leads to two sets of equations for the steady and unsteady motions.[14,25] The next step is to expand all unsteady variables in terms of the primary perturbation parameter, ε. Each fluctuation a' may hence be written as

$$a' = \varepsilon a^{(1)} + \varepsilon^2 a^{(2)} + \varepsilon^3 a^{(3)} + \mathcal{O}(\varepsilon^4) \tag{9}$$

Here a alludes to a generic flow variable, and ε denotes the ratio of the superimposed oscillatory pressure amplitude to the traditionally larger mean chamber pressure. After some algebra, the governing equations may be separated at first order in ε and rearranged as:

$$\begin{cases} \dfrac{\partial \rho^{(1)}}{\partial t} = -\nabla \cdot \boldsymbol{u}^{(1)} - M_b \nabla \cdot \left[\rho^{(1)} \boldsymbol{U} \right] \\ \dfrac{\partial \boldsymbol{u}^{(1)}}{\partial t} = -\dfrac{1}{\gamma} \nabla p^{(1)} - M_b \left\{ \nabla \left[\boldsymbol{U} \cdot \boldsymbol{u}^{(1)} \right] - \boldsymbol{U} \times \boldsymbol{\omega}^{(1)} - \boldsymbol{u}^{(1)} \times \bar{\boldsymbol{\Omega}} \right\} - \delta^2 \nabla \times \boldsymbol{\omega}^{(1)} + \delta_d^2 \nabla \left[\nabla \cdot \boldsymbol{u}^{(1)} \right] \\ \dfrac{\partial T^{(1)}}{\partial t} = -M_b \boldsymbol{U} \cdot \nabla T^{(1)} + \dfrac{\gamma - 1}{\gamma} \left[\dfrac{\partial p^{(1)}}{\partial t} + M_b \boldsymbol{U} \cdot \nabla p^{(1)} \right] + \dfrac{\delta^2}{Pr} \nabla^2 T^{(1)} \\ p^{(1)} = T^{(1)} + \rho^{(1)}; \quad p^{(1)} = \gamma \rho^{(1)} \end{cases} \tag{10}$$

Equation (10) is often referred to as the set of interaction equations in which the influence of the mean flowfield, $\boldsymbol{U}$, on the unsteady disturbances, $\boldsymbol{u}^{(1)}$, is clearly seen.

D. Headwall Injection Pattern

It may be instructive to note that the system of first-order interaction equations encapsulated above is strongly dependent on $\boldsymbol{U}$, the steady stream of incoming fluid across the headwall. In practice, the injection process at the faceplate can be somewhat complex, specifically when taking into account the multitude of possible injector configurations and showerhead patterns. Nonetheless, it is routinely assumed that a streamtube motion quickly develops, especially for conventional thrust chambers.[32] Bearing these factors in mind, only low-order representations of the incoming jet will be considered here. In the interest of simplicity, two types of injections will be employed. The first corresponds to a uniform, top-hat, plug flow along the chamber length, and the second implements a self-similar, bell-shaped, half-cosine that is often attributed to Berman.[28] The latter has been frequently used in theoretical studies of propulsive systems with headwall injection. Examples abound and one may cite, for example: Culick,[21] Brown *et al.*,[22] Proudman,[33] Beddini,[34] Chedevergne, Casalis and Féraille,[35] Griffond and Casalis,[36] Saad and Majdalani,[37] and Majdalani.[38] The two test cases may be represented in non-dimensional form using

Uniform profile:
$$\boldsymbol{U} = (0)\boldsymbol{e}_r + (0)\boldsymbol{e}_\theta + (1)\boldsymbol{e}_z \tag{11}$$

Berman (bell-shaped) profile:
$$\boldsymbol{U} = (0)\boldsymbol{e}_r + (0)\boldsymbol{e}_\theta + \cos\left(\tfrac{1}{2}\pi r^2\right)\boldsymbol{e}_z \tag{12}$$

In what follows, the vorticoacoustic transverse wave will be modeled in the presence of an oscillatory pressure disturbance and a mean flowfield corresponding to Eqs. (11)–(12).

E. Flowfield Decomposition

In comparable studies leading to analytical solutions of wave motions, first-order fluctuations are invariably separated into an acoustic and a vortical field.[39,40] On the one hand, the acoustic part produces a potential motion that is compressible, irrotational, inviscid and isentropic. On the other hand, the vortical part gives rise to an incompressible, rotational, and viscous field.[27] At the onset, the potential solution, being inviscid, proves incapable of satisfying the velocity adherence condition at solid boundaries. Both physically and mathematically, a correction is required, namely in the form of a vortical wave. The latter is generated at the boundary in such a manner as to offset the acoustic part at the wall. Using a circumflex to denote the pressure-driven potential part, and a tilde for the boundary-driven vortical component, the unsteady flow variables may be once more decomposed into:

$$\boldsymbol{u}^{(1)} = \hat{\boldsymbol{u}} + \tilde{\boldsymbol{u}}; \quad \boldsymbol{\omega}^{(1)} = \hat{\boldsymbol{\omega}} + \tilde{\boldsymbol{\omega}}; \quad p^{(1)} = \hat{p} + \tilde{p}; \quad \rho^{(1)} = \hat{\rho} + \tilde{\rho}; \quad T^{(1)} = \hat{T} + \tilde{T} \tag{13}$$

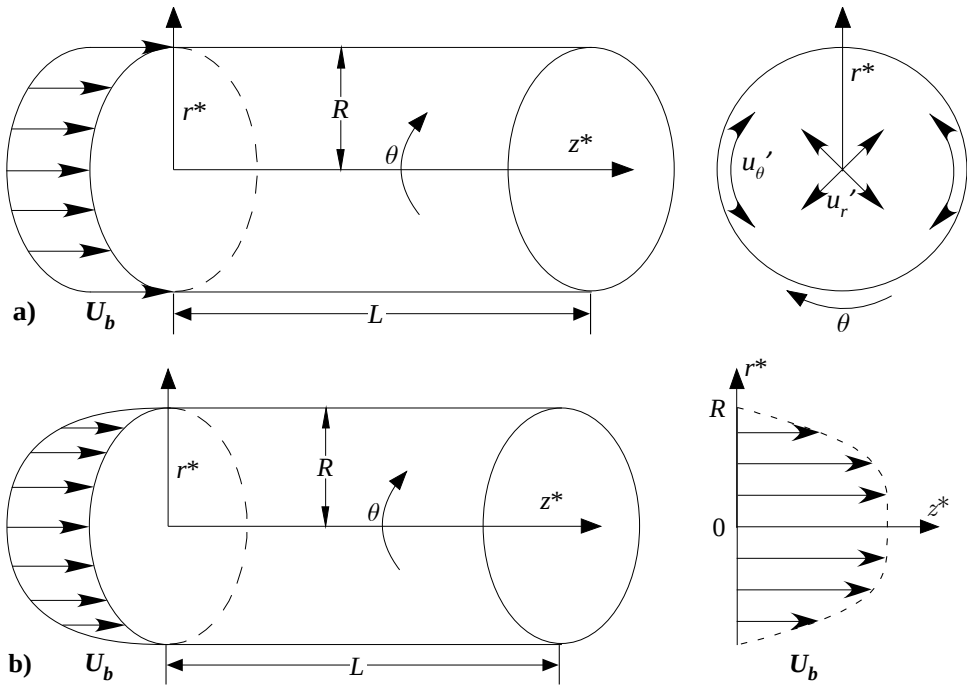

Figure 1. Chamber geometry and coordinate system showing a) uniform flow and b) bell-shaped profile. Also shown is a front view depicting the coupled tangential and radial wave motions that together dictate the transverse mode shapes.

Substituting Eq. (13) into Eq. (10) yields two independent sets of equations that remain coupled by virtue of the no-slip requirement that must be fulfilled along the headwall.[40] These are:

Acoustic set:
$$\begin{cases} \dfrac{\partial \hat{\rho}}{\partial t} = -\nabla\cdot\hat{\boldsymbol{u}} - M_b \boldsymbol{U}\nabla\cdot\hat{\rho}; \quad \dfrac{\partial \hat{\boldsymbol{u}}}{\partial t} = -\dfrac{1}{\gamma}\nabla\hat{p} - M_b\left[\nabla\left(\boldsymbol{U}\cdot\hat{\boldsymbol{u}}\right) - \hat{\boldsymbol{u}}\times\bar{\boldsymbol{\Omega}}\right] \\ \dfrac{\partial \hat{T}}{\partial t} = -M_b\boldsymbol{U}\cdot\nabla\hat{T} + \dfrac{\gamma-1}{\gamma}\left(\dfrac{\partial \hat{p}}{\partial t} + M_b\boldsymbol{U}\cdot\nabla\hat{p}\right) \\ \hat{p} = \hat{T} + \hat{\rho}; \quad \hat{p} = \gamma\hat{\rho} \end{cases} \tag{14}$$

Vortical set:
$$\begin{cases} \nabla\cdot\tilde{\boldsymbol{u}} = 0; \quad \dfrac{\partial \tilde{\boldsymbol{u}}}{\partial t} = -\dfrac{1}{\gamma}\nabla\tilde{p} - M_b\left[\nabla\left(\boldsymbol{U}\cdot\tilde{\boldsymbol{u}}\right) - \boldsymbol{U}\times\tilde{\boldsymbol{\omega}} - \tilde{\boldsymbol{u}}\times\bar{\boldsymbol{\Omega}}\right] - \delta^2\nabla\times\tilde{\boldsymbol{\omega}} + \delta_d^2\nabla\left(\nabla\cdot\tilde{\boldsymbol{u}}\right) \\ \dfrac{\partial \tilde{T}}{\partial t} = -M_b\boldsymbol{U}\cdot\nabla\tilde{T} + \dfrac{\gamma-1}{\gamma}\left(\dfrac{\partial \tilde{p}}{\partial t} + M_b\boldsymbol{U}\cdot\nabla\tilde{p}\right) + \dfrac{\delta^2}{Pr}\nabla^2\tilde{T} \\ \tilde{p} = \tilde{T} + \tilde{\rho} \end{cases} \tag{15}$$

F. Boundary Conditions

The fundamental disparities between acoustic and vortical fields warrant the use of two dissimilar sets of boundary conditions. In the case of the acoustic wave, a closed boundary must be maintained, as usual, along all solid surfaces, including the injection site (i.e., at $r = 1$, $z = 0$ and $z = L/R$). In the case of the rotational wave, the no-slip condition at the headwall must be secured first and foremost, being the counterpart of the sidewall boundary in the inverted analog of an axially traveling wave within an elongated porous cylinder.[18,40] In both geometric configurations, the velocity adherence constraint is imposed at the injecting surfaces, and these correspond to either the headwall or the sidewall of the simulated LRE and SRM, respectively. Along the non-injecting surface (sidewall), slip may be allowed in the vortical wave formulation. At the downstream end of the chamber, $z = L/R$, the vortical wave must remain bounded and, being sufficiently removed from the headwall, its rotational effects are expected to have died out. Naturally, with the attenuation of the unsteady vorticity component, the vorticoacoustic wave reduces to its potential form. A summary of the physical constraints entailed in the resulting model is given in Table 1.

III. Solution

This section describes the boundary layer approach that we follow to reduce the time-dependent vortical system into a more manageable set. The ensuing formulations are provided for both mean flow profiles. However, because the vortical field is engendered by the acoustic wave, the latter must be considered first.

A. Acoustic Formulation

Although Eq. (14) consists of an assortment of five equations, it can be systematically reduced to a single equation that represents a modified form of the wave equation. Using a well-established manipulation of the acoustic set, the time derivative of the acoustic mass conservation may be subtracted from the divergence of the corresponding momentum equation to arrive at an extended form of the wave equation:[18]

$$\frac{\partial^2 \hat{p}}{\partial t^2} = \nabla^2\hat{p} + M_b\left[\gamma\nabla^2\left(\boldsymbol{U}\cdot\hat{\boldsymbol{u}}\right) - \gamma\nabla\cdot\left(\hat{\boldsymbol{u}}\times\bar{\boldsymbol{\Omega}}\right) - \frac{\partial}{\partial t}\left(\boldsymbol{U}\nabla\cdot\hat{p}\right)\right] \tag{16}$$

Note that Eq. (16) incorporates the effects of the mean flow, albeit at the order of the blowing Mach number. At this juncture, it may be useful to recall that the inlet or blowing Mach number is usually smaller than unity $\left(M_b \le 0.3 \ll 1\right)$. As such, it may be used as a secondary perturbation parameter. This enables us to expand the acoustic pressure in successive powers of M_b, namely,

Table 1. Boundary conditions for the acoustic and vortical fields

	Boundary		
	$r = 1$	$z = 0$	$z = L/R$
Acoustic field	$\mathbf{n}\cdot\nabla\hat{p} = 0$	$\mathbf{n}\cdot\nabla\hat{p} = 0$	$\mathbf{n}\cdot\nabla\hat{p} = 0$
Vortical field	no condition imposed	$u_r' = u_\theta' = u_z' = 0$	bounded

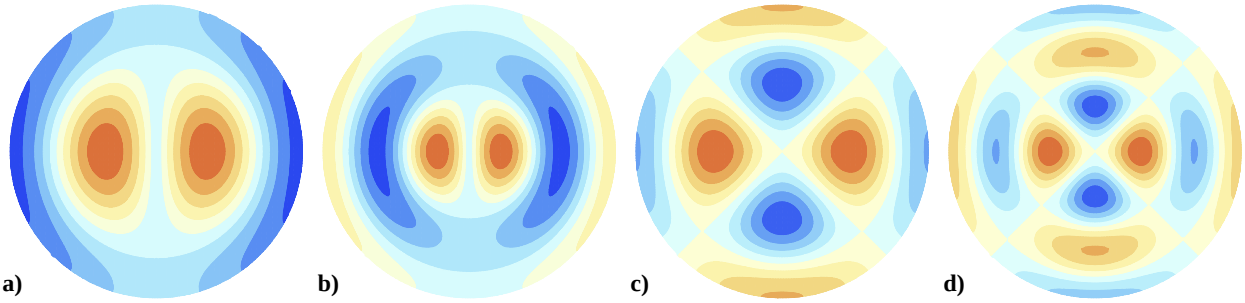

Figure 2. Pressure contours in a polar slice for transverse oscillations corresponding to: a) K_{11}, b) K_{12}, c) K_{21} and d) K_{22}.

$$\hat{p} = \hat{p}^{(0)} + M_b \hat{p}^{(1)} + M_b^2 \hat{p}^{(2)} + \mathcal{O}(M_b{}^3) \tag{17}$$

Forthwith, backward substitution into Eq. (16) renders, at leading order,

$$\frac{\partial^2 \hat{p}^{(0)}}{\partial t^2} = \nabla^2 \hat{p}^{(0)} \tag{18}$$

We thus recover the classical wave equation in three dimensions. The solution of this partial differential equation (PDE) may be readily extracted using separation of variables. One gets

$$\hat{p}^{(0)}(t,r,\theta,z) = e^{-iK_{mn}t} J_m(K_{mn} r)\cos(m\theta)\cos(K_l z) \tag{19}$$

where m, n and l are positive integers that refer to the tangential, radial, and longitudinal mode numbers, respectively. In the same vein, K_{mn} designates the transverse wave number that depends on the joint tangential and radial modes, m and n. In practice, it is deduced numerically by solving $J'_m(K_{mn}) = 0$ and generating, in successive fashion,[18] the first radial, first tangential, first radial and tangential modes, etc., according to:

$$\begin{cases} K_{01} \approx 3.831\,705\,97 & K_{10} \approx 1.841\,183\,78 & K_{11} \approx 5.331\,442\,77 \\ K_{02} \approx 7.015\,586\,67 & K_{20} \approx 3.054\,236\,93 & K_{22} \approx 9.969\,467\,82 \\ K_{12} \approx 8.536\,316\,37 & K_{21} \approx 6.706\,133\,19 & \textit{etc.} \end{cases} \tag{20}$$

To simplify the forthcoming analysis, we note that for a short cylindrical enclosure in general, or a simulated LRE in particular, the tangential and radial oscillations tend to dominate over their longitudinal counterpart, mainly due to the short length of the chamber. Hence, in our effort to emphasize the contribution of the transverse modes, and given that $\cos(K_l z)$ remains close to unity for small z, the axial wave number K_l is deliberately set to zero. The leading-order acoustic pressure becomes

$$\hat{p}^{(0)}(t,r,\theta,z) = e^{-iK_{mn}t} J_m(K_{mn} r)\cos(m\theta) \tag{21}$$

The corresponding acoustic velocity may be deduced by integrating the momentum equation and evaluating

$$\hat{\boldsymbol{u}}^{(0)} = -\frac{1}{\gamma}\int \nabla \hat{p}^{(0)} \mathrm{d}t \tag{22}$$

A complete leading-order acoustic solution may hence be realized, specifically

$$\begin{cases} \hat{p} = e^{-iK_{mn}t} J_m(K_{mn} r)\cos(m\theta); \quad \hat{u}_r = \dfrac{i}{K_{mn}\gamma} e^{-iK_{mn}t} J'_m(K_{mn} r)\cos(m\theta) \\ \hat{u}_\theta = \dfrac{i}{K_{mn}\gamma}\dfrac{m}{r} e^{-iK_{mn}t} J_m(K_{mn} r)\sin(m\theta); \quad \hat{u}_z = 0 \end{cases} \tag{23}$$

In Eq. (23) and what follows, a prime implies differentiation with respect to the radial coordinate, $\partial/\partial r$.

For the reader's convenience, the four parts of Fig. 2 are used to illustrate the instantaneous pressure distribution in our cylindrical chamber at four sequential mode numbers. These correspond to four zeroes of J'_m that are enumerated in Eq. (20). Everywhere, the pressure contours represent snapshots taken in a polar plane at $t = 0.01\,\mathrm{s}, \forall z$, where red and blue colors (online) denote high and low values, respectively. It is interesting to note the evolution of the nodal lines going from a) to d), thus giving rise to double-D and alternating cross patterns that characterize the acoustic modes shapes. In a) and b), the first and second radial modes are featured along with the first tangential mode where alternating double-D contours appear either a) once or b) twice, with the second set brushing along the outer periphery. In c) and d), the second tangential configuration is depicted at the first and

second radial modes. The last contour clearly captures the symmetrically alternating wave structure in both tangential and radial directions.

B. Vortical Formulation

Before proceeding with the solution of the vortical disturbance, it may be useful to clarify the origin of the driving mechanisms for the waves in question, while paying special attention to the reason for the decoupling of the incompressible continuity and momentum equations from the remaining members in Eq. (15). To this end, we recall that the acoustic wave is driven by the pressure differential in the chamber but remains uninfluenced by the no-slip requirement at the boundaries or the mean flow at the leading order in M_b. In contrast, the vortical waves are driven by the acoustic motion at the boundaries and appear only as a dissipating correction to the latter that is impacted by the chamber's geometry, the mean flow, and the acoustic field. It may hence be argued that the ensuing vortical pressure differential may be dismissed in view of the pressure differential being mainly provided by the acoustic field. This assumption enables us to ignore $\tilde{p}$ as a first approximation in the momentum equation and reduce the remaining set into[14]

$$\begin{cases} \nabla\cdot\tilde{\boldsymbol{u}}=0 \\ \dfrac{\partial\tilde{\boldsymbol{u}}}{\partial t}=-M_b\left[\nabla\left(\boldsymbol{U}\cdot\tilde{\boldsymbol{u}}\right)-\boldsymbol{U}\times\tilde{\boldsymbol{\omega}}-\tilde{\boldsymbol{u}}\times\bar{\boldsymbol{\Omega}}\right]-\delta^2\nabla\times\tilde{\boldsymbol{\omega}} \end{cases} \tag{24}$$

Interestingly, the system in Eq. (24) becomes over-determined, being comprised of four equations with three unknowns: the three velocity components, $\tilde{u}_r$, $\tilde{u}_\theta$ and $\tilde{u}_z$. A solution based on any three equations has the propensity to generate a large error in the fourth equation, depending on which three are chosen. To mathematically close the system, one can retain the small vortical pressure wave $\tilde{p}$ in the momentum equation. The amended set becomes:

$$\begin{cases} \nabla\cdot\tilde{\boldsymbol{u}}=0 \\ \dfrac{\partial\tilde{\boldsymbol{u}}}{\partial t}=-\dfrac{1}{\gamma}\nabla\tilde{p}-M_b\left[\nabla\left(\boldsymbol{U}\cdot\tilde{\boldsymbol{u}}\right)-\boldsymbol{U}\times\tilde{\boldsymbol{\omega}}-\tilde{\boldsymbol{u}}\times\bar{\boldsymbol{\Omega}}\right]-\delta^2\nabla\times\tilde{\boldsymbol{\omega}} \end{cases} \tag{25}$$

In seeking an ansatz for $\tilde{\boldsymbol{u}}$, we note that in Eq. (25), the rotational velocity disturbance stands as a function of time and three spatial variables. Moreover, $\tilde{\boldsymbol{u}}\left(t,r,\theta,z\right)$ must be chosen in a manner to identically cancel the acoustic motion at the headwall, $\forall t$. The time dependence of the vortical field must therefore match that of the acoustic motion at the headwall. This can be achieved when the unsteady vortical wave exhibits the form:

$$\tilde{\boldsymbol{u}}=e^{-iK_{mn}t}f\left(r,\theta,z\right)\quad\text{or}\quad\frac{\partial\tilde{\boldsymbol{u}}}{\partial t}=-iK_{mn}e^{-iK_{mn}t}f\left(r,\theta,z\right)=-iK_{mn}\tilde{\boldsymbol{u}} \tag{26}$$

This ansatz will be later used to secure a closed-form vortical approximation.

C. Uniform Mean Flow

The transverse wave subject to a uniform mean flow has been briefly explored by Fischbach, Flandro and Majdalani[18] in their investigation of the acoustic streaming mechanism in a simulated LRE. The present approach applies a regular perturbation expansion to a well-established variant of the conservation equations. For the case of a uniform mean flow, Eq. (25) may be expanded in scalar notation to produce

$$\begin{cases} \dfrac{\tilde{u}_r}{r}+\dfrac{\partial\tilde{u}_r}{\partial r}+\dfrac{1}{r}\dfrac{\partial\tilde{u}_\theta}{\partial\theta}+\dfrac{\partial\tilde{u}_z}{\partial z}=0 \\ -iK_{mn}\tilde{u}_r+M_b\dfrac{\partial\tilde{u}_r}{\partial z}=-\dfrac{1}{\gamma}\dfrac{\partial\tilde{p}}{\partial r}+\delta^2\left(\dfrac{\partial^2\tilde{u}_r}{\partial z^2}+\dfrac{1}{r^2}\dfrac{\partial^2\tilde{u}_r}{\partial\theta^2}-\dfrac{1}{r^2}\dfrac{\partial\tilde{u}_\theta}{\partial\theta}-\dfrac{1}{r}\dfrac{\partial^2\tilde{u}_\theta}{\partial r\partial\theta}-\dfrac{\partial^2\tilde{u}_z}{\partial r\partial z}\right) \\ -iK_{mn}\tilde{u}_\theta+M_b\dfrac{\partial\tilde{u}_\theta}{\partial z}=-\dfrac{1}{\gamma r}\dfrac{\partial\tilde{p}}{\partial\theta}+\delta^2\left(\dfrac{1}{r^2}\dfrac{\partial\tilde{u}_r}{\partial\theta}-\dfrac{1}{r}\dfrac{\partial^2\tilde{u}_r}{\partial r\partial\theta}-\dfrac{\tilde{u}_\theta}{r^2}+\dfrac{\partial^2\tilde{u}_\theta}{\partial z^2}+\dfrac{1}{r}\dfrac{\partial\tilde{u}_\theta}{\partial r}+\dfrac{\partial^2\tilde{u}_\theta}{\partial r^2}-\dfrac{1}{r}\dfrac{\partial^2\tilde{u}_z}{\partial\theta\partial z}\right) \\ -iK_{mn}\tilde{u}_z+M_b\dfrac{\partial\tilde{u}_z}{\partial z}=-\dfrac{1}{\gamma}\dfrac{\partial\tilde{p}}{\partial z}-\delta^2\left(\dfrac{1}{r}\dfrac{\partial\tilde{u}_r}{\partial z}+\dfrac{\partial^2\tilde{u}_r}{\partial r\partial z}+\dfrac{1}{r}\dfrac{\partial^2\tilde{u}_\theta}{\partial\theta\partial z}-\dfrac{1}{r^2}\dfrac{\partial^2\tilde{u}_z}{\partial\theta^2}-\dfrac{1}{r}\dfrac{\partial\tilde{u}_z}{\partial r}-\dfrac{\partial^2\tilde{u}_z}{\partial r^2}\right) \end{cases} \tag{27}$$

Recognizing that the vortical wave is dominant near the boundaries, Eq. (27) may be transformed using boundary layer theory, with the no-slip boundary condition being enforced at the headwall. Because the vortical wave can grow or decay in the axial direction, we rescale the axial variable using a stretched inner coordinate

$$\zeta = \frac{z}{\delta} \tag{28}$$

The next step is to perturb the vortical variables that appear in Eq. (27) with respect to the viscous parameter using

$$\tilde{a} = \tilde{a}^{(0)} + \delta\tilde{a}^{(1)} + \delta^2\tilde{a}^{(2)} + \delta^3\tilde{a}^{(3)} + \mathcal{O}(\delta^4) \tag{29}$$

Collecting terms of the same order in δ and rearranging leads to two vortical sets that must be solved successively.

1. Leading-Order Solution

At $\mathcal{O}(1)$, Eq. (27) begets

$$\frac{\partial\tilde{u}_\zeta^{(0)}}{\partial\zeta} = 0 \tag{30}$$

$$-iK_{mn}\tilde{u}_r^{(0)} + \frac{M_b}{\delta}\frac{\partial\tilde{u}_r^{(0)}}{\partial\zeta} - \frac{\partial^2\tilde{u}_r^{(0)}}{\partial\zeta^2} = -\frac{1}{\gamma}\frac{\partial\tilde{p}^{(0)}}{\partial r} \tag{31}$$

$$-iK_{mn}\tilde{u}_\theta^{(0)} + \frac{M_b}{\delta}\frac{\partial\tilde{u}_\theta^{(0)}}{\partial\zeta} - \frac{\partial^2\tilde{u}_\theta^{(0)}}{\partial\zeta^2} = -\frac{1}{\gamma r}\frac{\partial\tilde{p}^{(0)}}{\partial\theta} \tag{32}$$

$$\frac{1}{\gamma}\frac{\partial\tilde{p}^{(0)}}{\partial\zeta} = 0 \tag{33}$$

From one angle, solving Eq. (33) yields an axially invariant $\tilde{p}^{(0)}$ that is only a function of the radial, tangential and time variables. The axial propagation of the vortical wave is thus driven solely by the no-slip condition at the headwall. At this order, the vortical pressure does not affect the wave generated and must be set equal to zero to preserve the physicality of the case at hand. Similarly, Eq. (30) leads to a vanishing leading-order axial velocity contribution. We collect:

$$\tilde{p}^{(0)} = 0; \quad \tilde{u}_\zeta^{(0)} = 0 \tag{34}$$

From another angle, the solutions of Eqs. (31) and (32) may be straightforwardly extracted. The radial now-homogeneous partial differential equation (PDE) precipitates

$$\tilde{u}_r^{(0)} = A_{r0}(t,r,\theta)e^{X_1\zeta} + B_{r0}(t,r,\theta)e^{X_2\zeta} \tag{35}$$

where

$$X_1 = \frac{M_b}{2\delta}\left(1 - \sqrt{1 - \frac{4iK_{mn}\delta^2}{M_b^2}}\right) = \frac{M_b}{2\delta}\left(1 - \sqrt{\frac{1}{2} + \frac{1}{2}\sqrt{1 + \frac{16K_{mn}^2\delta^4}{M_b^4}}} + i\sqrt{\frac{1}{2}\sqrt{1 + \frac{16K_{mn}^2\delta^4}{M_b^4}} - \frac{1}{2}}\right) \tag{36}$$

$$X_2 = \frac{M_b}{2\delta}\left(1 + \sqrt{1 - \frac{4iK_{mn}\delta^2}{M_b^2}}\right) = \frac{M_b}{2\delta}\left(1 + \sqrt{\frac{1}{2} + \frac{1}{2}\sqrt{1 + \frac{16K_{mn}^2\delta^4}{M_b^4}}} - i\sqrt{\frac{1}{2}\sqrt{1 + \frac{16K_{mn}^2\delta^4}{M_b^4}} - \frac{1}{2}}\right) \tag{37}$$

At this juncture, two physical constraints may be brought to bear: the physicality of the solution in the farfield and the no-slip requirement at the headwall. First, because the real part of X_2 is positive, $B_{r0}(r,\theta,t)$ must be suppressed to prevent the unbounded, unphysical growth of the velocity as ζ tends to infinity. Equation (35) reduces to

$$\tilde{u}_r^{(0)} = A_{r0}(t,r,\theta)e^{X_1\zeta} \tag{38}$$

Second, the velocity adherence condition at the headwall ($\zeta = 0$) demands that

$$\tilde{u}_r^{(0)}(t,r,\theta,0) + \hat{u}_r(t,r,\theta,0) = 0 \tag{39}$$

and so

$$A_{r0}(t,r,\theta) = -\frac{i}{K_{mn}\gamma}e^{-iK_{mn}t}\cos(m\theta)J_m'(K_{mn}r) \tag{40}$$

or

$$\tilde{u}_r^{(0)} = -\frac{i}{K_{mn}\gamma}e^{-iK_{mn}t}e^{X_1\zeta}\cos(m\theta)J_m'(K_{mn}r) \tag{41}$$

A similar procedure can be used to solve Eq. (32) with the outcome being

$$\tilde{u}_\theta^{(0)} = -\frac{i}{K_{mn}\gamma}\frac{m}{r}e^{-iK_{mn}t}e^{X_1\zeta}\sin(m\theta)J_m(K_{mn}r) \tag{42}$$

2. First-Order Solution

At $\mathcal{O}(\delta)$, Eq. (27) yields

$$\frac{\partial \tilde{u}_\zeta^{(1)}}{\partial \zeta} = -\frac{1}{r}\tilde{u}_r^{(0)} - \frac{\partial \tilde{u}_r^{(0)}}{\partial r} - \frac{1}{r}\frac{\partial \tilde{u}_\theta^{(0)}}{\partial \theta} \tag{43}$$

$$iK_{mn}\tilde{u}_r^{(1)} - \frac{M_b}{\delta}\frac{\partial \tilde{u}_r^{(1)}}{\partial \zeta} + \frac{\partial^2 \tilde{u}_r^{(1)}}{\partial \zeta^2} = \frac{1}{\gamma}\frac{\partial \tilde{p}^{(1)}}{\partial r} + \frac{\partial^2 \tilde{u}_\zeta^{(0)}}{\partial r \partial \zeta} \tag{44}$$

$$iK_{mn}\tilde{u}_\theta^{(1)} - \frac{M_b}{\delta}\frac{\partial \tilde{u}_\theta^{(1)}}{\partial \zeta} + \frac{\partial^2 \tilde{u}_\theta^{(1)}}{\partial \zeta^2} = -\frac{1}{\gamma r}\frac{\partial \tilde{p}^{(1)}}{\partial \theta} + \frac{1}{r}\frac{\partial^2 \tilde{u}_\zeta^{(0)}}{\partial \theta \partial \zeta} \tag{45}$$

$$\frac{1}{\gamma}\frac{\partial \tilde{p}^{(1)}}{\partial \zeta} = iK_{mn}\tilde{u}_\zeta^{(0)} - \frac{M_b}{\delta}\frac{\partial \tilde{u}_\zeta^{(0)}}{\partial \zeta} \tag{46}$$

The vanishing leading-order axial velocity leads to a null first-order pseudo-pressure. Subsequently, Eq. (44) reduces to

$$iK_{mn}\tilde{u}_r^{(1)} - \frac{M_b}{\delta}\frac{\partial \tilde{u}_r^{(1)}}{\partial \zeta} + \frac{\partial^2 \tilde{u}_r^{(1)}}{\partial \zeta^2} = 0 \tag{47}$$

The solution of this homogenous PDE is analogous to that of Eq. (38), namely,

$$\tilde{u}_r^{(1)} = A_{r1}(t, r, \theta)e^{X_1 \zeta} \tag{48}$$

Here too, the no-slip condition must be fulfilled. However, since the cancellation of the acoustic velocity has been accomplished at the previous order, the leading-order contribution at the headwall must not interfere. This implies

$$\tilde{u}_r^{(1)}(t, r, \theta, 0) = 0 \tag{49}$$

Equation (49) results in a vanishing first-order radial velocity. A parallel procedure applies to the tangential component in Eq. (45), which mirrors Eq. (44). The first-order tangential velocity is also found to be zero. We hence realize

$$\tilde{u}_r^{(1)} = \tilde{u}_\theta^{(1)} = 0 \tag{50}$$

At this point, the axial component may be resolved. By substituting Eqs. (41) and (42) into Eq. (43), we obtain

$$\frac{\partial \tilde{u}_\zeta^{(1)}}{\partial \zeta} = \frac{iK_{mn}}{\gamma}e^{-iK_{mn}t}e^{X_1 \zeta}\cos(m\theta)J_m(K_{mn}r) \tag{51}$$

Equation (51) may be integrated and made to satisfy the headwall boundary condition. This operation involves

$$\tilde{u}_\zeta^{(1)} = \frac{iK_{mn}}{\gamma}e^{-iK_{mn}t}\frac{e^{X_1 \zeta}}{X_1}\cos(m\theta)J_m(K_{mn}r) + A_{\zeta 1}(t, r, \theta) \tag{52}$$

and

$$\tilde{u}_\zeta^{(1)}(t, r, \theta, 0) = 0 \quad \text{or} \quad A_{\zeta 1}(t, r, \theta) = -\frac{iK_{mn}}{\gamma}\frac{1}{X_1}e^{-iK_{mn}t}\cos(m\theta)J_m(K_{mn}r) \tag{53}$$

whence

$$\tilde{u}_\zeta^{(1)} = \frac{iK_{mn}}{\gamma}\frac{1}{X_1}e^{-iK_{mn}t}\cos(m\theta)J_m(K_{mn}r)\left(e^{X_1 \zeta} - 1\right) \tag{54}$$

D. Bell-Shaped Mean Flow

It may be argued that the one-dimensional bell-shaped mean flow stands to provide a better physical approximation to the real phenomenon. While the uniform profile allows for slippage at the boundary, the bell-shaped motion overcomes this deficiency by forcing the fluid to slow down to zero at the sidewall. Through the use of a more realistic representation of the mean flow, an improved solution for the transverse oscillations may hence be achieved. In this case, the expansion of Eq. (25) produces

$$\frac{\tilde{u}_r}{r} + \frac{\partial \tilde{u}_r}{\partial r} + \frac{1}{r}\frac{\partial \tilde{u}_\theta}{\partial \theta} + \frac{\partial \tilde{u}_z}{\partial z} = 0 \tag{55}$$

$$-iK_{mn}\tilde{u}_r + M_b \cos\left(\tfrac{1}{2}\pi r^2\right)\frac{\partial \tilde{u}_r}{\partial z} = -\frac{1}{\gamma}\frac{\partial \tilde{p}}{\partial r} + \delta^2\left(\frac{\partial^2 \tilde{u}_r}{\partial z^2} + \frac{1}{r^2}\frac{\partial^2 \tilde{u}_r}{\partial \theta^2} - \frac{1}{r^2}\frac{\partial \tilde{u}_\theta}{\partial \theta} - \frac{1}{r}\frac{\partial^2 \tilde{u}_\theta}{\partial r \partial \theta} - \frac{\partial^2 \tilde{u}_z}{\partial r \partial z}\right) \tag{56}$$

$$-iK_{mn}\tilde{u}_\theta + M_b \cos\left(\tfrac{1}{2}\pi r^2\right)\frac{\partial \tilde{u}_\theta}{\partial z} = -\frac{1}{\gamma r}\frac{\partial \tilde{p}}{\partial \theta} + \delta^2\left(\frac{1}{r^2}\frac{\partial \tilde{u}_r}{\partial \theta} - \frac{1}{r}\frac{\partial^2 \tilde{u}_r}{\partial r \partial \theta} - \frac{\tilde{u}_\theta}{r^2} + \frac{\partial^2 \tilde{u}_\theta}{\partial z^2} + \frac{1}{r}\frac{\partial \tilde{u}_\theta}{\partial r} + \frac{\partial^2 \tilde{u}_\theta}{\partial r^2} - \frac{1}{r}\frac{\partial^2 \tilde{u}_z}{\partial \theta \partial z}\right) \tag{57}$$

$$\begin{aligned} -iK_{mn}\tilde{u}_z + M_b \cos\left(\tfrac{1}{2}\pi r^2\right)\frac{\partial \tilde{u}_z}{\partial z} - M_b \pi r \sin\left(\tfrac{1}{2}\pi r^2\right)\tilde{u}_r \\ = -\frac{1}{\gamma}\frac{\partial \tilde{p}}{\partial z} + \delta^2\left(-\frac{1}{r}\frac{\partial \tilde{u}_r}{\partial z} - \frac{\partial^2 \tilde{u}_r}{\partial r \partial z} - \frac{1}{r}\frac{\partial^2 \tilde{u}_\theta}{\partial \theta \partial z} + \frac{1}{r^2}\frac{\partial^2 \tilde{u}_z}{\partial \theta^2} + \frac{1}{r}\frac{\partial \tilde{u}_z}{\partial r} + \frac{\partial^2 \tilde{u}_z}{\partial r^2}\right) \end{aligned} \tag{58}$$

The next step is to invoke boundary layer theory to stretch the axial coordinate and reduce Eqs. (55)–(58) asymptotically by perturbing the resulting set with respect to δ.

1. Leading-Order Solution

Using $\zeta = z/\delta$ and a series after Eq. (29), Eqs. (55)–(58) may be expanded and segregated at $\mathcal{O}(1)$ into

$$\frac{\partial \tilde{u}_\zeta^{(0)}}{\partial \zeta} = 0 \tag{59}$$

$$-iK_{mn}\tilde{u}_r^{(0)} + \frac{M_b}{\delta}\cos\left(\tfrac{1}{2}\pi r^2\right)\frac{\partial \tilde{u}_r^{(0)}}{\partial \zeta} - \frac{\partial^2 \tilde{u}_r^{(0)}}{\partial \zeta^2} = -\frac{1}{\gamma}\frac{\partial \tilde{p}^{(0)}}{\partial r} \tag{60}$$

$$-iK_{mn}\tilde{u}_\theta^{(0)} + \frac{M_b}{\delta}\cos\left(\tfrac{1}{2}\pi r^2\right)\frac{\partial \tilde{u}_\theta^{(0)}}{\partial \zeta} - \frac{\partial^2 \tilde{u}_\theta^{(0)}}{\partial \zeta^2} = -\frac{1}{\gamma r}\frac{\partial \tilde{p}^{(0)}}{\partial \theta} \tag{61}$$

$$\frac{1}{\gamma}\frac{\partial \tilde{p}^{(0)}}{\partial \zeta} = 0 \tag{62}$$

The treatment of Eqs. (62) then (59) mirrors the case of uniform injection. The leading-order pseudo-pressure and axial velocity are both determined to be vanishingly small, or $\tilde{p}^{(0)} = \tilde{u}_\zeta^{(0)} = 0$. However, the solution of Eq. (60) leaves us with

$$\tilde{u}_r^{(0)} = A_r(t,r,\theta)e^{X_{1C}\zeta} + B_r(t,r,\theta)e^{X_{2C}\zeta} \tag{63}$$

where

$$X_{1C}(r) = \frac{M_b}{2\delta}\left[1 - \sqrt{1 - \frac{4iK_{mn}\delta^2}{M_b^2\cos^2\left(\tfrac{1}{2}\pi r^2\right)}}\right] = \frac{M_b}{2\delta}\left[1 - \sqrt{\frac{1}{2} + \frac{1}{2}\sqrt{1 + \frac{16K_{mn}^2\delta^4}{M_b^4\cos^4\left(\tfrac{1}{2}\pi r^2\right)}}} + i\sqrt{\frac{1}{2}\sqrt{1 + \frac{16K_{mn}^2\delta^4}{M_b^4\cos^4\left(\tfrac{1}{2}\pi r^2\right)}} - \frac{1}{2}}\right] \tag{64}$$

$$X_{2C}(r) = \frac{M_b}{2\delta}\left[1 + \sqrt{1 - \frac{4iK_{mn}\delta^2}{M_b^2\cos^2\left(\tfrac{1}{2}\pi r^2\right)}}\right] = \frac{M_b}{2\delta}\left[1 + \sqrt{\frac{1}{2} + \frac{1}{2}\sqrt{1 + \frac{16K_{mn}^2\delta^4}{M_b^4\cos^4\left(\tfrac{1}{2}\pi r^2\right)}}} - i\sqrt{\frac{1}{2}\sqrt{1 + \frac{16K_{mn}^2\delta^4}{M_b^4\cos^4\left(\tfrac{1}{2}\pi r^2\right)}} - \frac{1}{2}}\right] \tag{65}$$

Because all cosine terms remain positive in the domain of interest, the real part of X_{2C} stays positive as well. Consequently, one must set $B_r(t,r,\theta) = 0$ to mitigate the exponential growth of $\tilde{u}_r^{(0)}$ as $\zeta \to \infty$ at the outer edge of the boundary layer region. This implies

$$\tilde{u}_r^{(0)} = A_{r0}(t,r,\theta)e^{X_{1C}\zeta} \tag{66}$$

Lastly, prevention of slippage at the headwall enables us to deduce $A_{r0}(t,r,\theta)$ and, therefore,

$$\tilde{u}_r^{(0)} = -\frac{i}{K_{mn}\gamma}e^{-iK_{mn}t}e^{X_{1C}\zeta}\cos(m\theta)J_m'(K_{mn}r) \tag{67}$$

A nearly identical procedure leads to the identification of the tangential component, specifically

$$\tilde{u}_\theta^{(0)} = -\frac{i}{K_{mn}\gamma}\frac{m}{r}e^{-iK_{mn}t}e^{X_{1C}\zeta}\sin(m\theta)J_m(K_{mn}r) \tag{68}$$

2. First-Order Solution

The first-order expansion of Eqs. (55)–(58) precipitates

$$\frac{\partial \tilde{u}_\zeta^{(1)}}{\partial \zeta} = -\frac{1}{r}\tilde{u}_r^{(0)} - \frac{\partial \tilde{u}_r^{(0)}}{\partial r} - \frac{1}{r}\frac{\partial \tilde{u}_\theta^{(0)}}{\partial \theta} \tag{69}$$

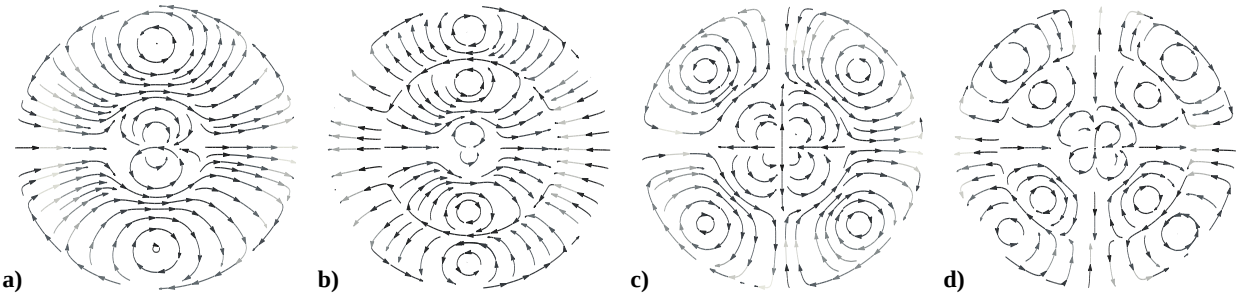

Figure 3. Vorticoacoustic velocity vectors in a polar slice taken at z=10^{-4} and a transverse mode number corresponding to: a) K_{11}=5.3314, b) K_{12}=8.5363, c) K_{21}=6.7061 and d) K_{22}=9.9695.

$$iK_{mn}\tilde{u}_r^{(1)} - \frac{M_b}{\delta}\cos\left(\tfrac{1}{2}\pi r^2\right)\frac{\partial \tilde{u}_r^{(1)}}{\partial \zeta} + \frac{\partial^2 \tilde{u}_r^{(1)}}{\partial \zeta^2} = \frac{1}{\gamma}\frac{\partial \tilde{p}^{(1)}}{\partial r} + \frac{\partial^2 \tilde{u}_\zeta^{(0)}}{\partial r \partial \zeta} \tag{70}$$

$$iK_{mn}\tilde{u}_\theta^{(1)} - \frac{M_b}{\delta}\cos\left(\tfrac{1}{2}\pi r^2\right)\frac{\partial \tilde{u}_\theta^{(1)}}{\partial \zeta} + \frac{\partial^2 \tilde{u}_\theta^{(1)}}{\partial \zeta^2} = -\frac{1}{\gamma}\frac{1}{r}\frac{\partial \tilde{p}^{(1)}}{\partial \theta} + \frac{1}{r}\frac{\partial^2 \tilde{u}_\zeta^{(0)}}{\partial \theta \partial \zeta} \tag{71}$$

$$\frac{1}{\gamma}\frac{\partial \tilde{p}^{(1)}}{\partial \zeta} = iK_{mn}\tilde{u}_\zeta^{(0)} - \frac{M_b}{\delta}\cos\left(\tfrac{1}{2}\pi r^2\right)\frac{\partial \tilde{u}_\zeta^{(0)}}{\partial \zeta} \tag{72}$$

By virtue of $\tilde{u}_\zeta^{(0)} = 0$, Eq. (72) can be solved to obtain $\tilde{p}^{(1)} = 0.$ The outcome may be substituted into Eq. (70) to arrive at a second-order homogeneous PDE in $\tilde{u}_r^{(1)}$, namely,

$$iK_{mn}\tilde{u}_r^{(1)} - \frac{M_b}{\delta}\cos\left(\tfrac{1}{2}\pi r^2\right)\frac{\partial \tilde{u}_r^{(1)}}{\partial \zeta} + \frac{\partial^2 \tilde{u}_r^{(1)}}{\partial \zeta^2} = 0 \tag{73}$$

The physical solution of Eq. (73) mirrors its counterpart at leading order with

$$\tilde{u}_r^{(1)} = A_{r1}(t, r, \theta)e^{X_{1C}\zeta} \tag{74}$$

Consistently with the uniform flow case, we can deduce that $\tilde{u}_r^{(1)} = \tilde{u}_\theta^{(1)} = 0$. Lastly, to extract the axial correction, Eqs. (67) and (68) may be inserted into Eq. (69) to retrieve

$$\frac{\partial \tilde{u}_\zeta^{(1)}}{\partial \zeta} = \frac{i}{\gamma K_{mn}}e^{-iK_{mn}t}\left[K_{mn}^2 J_m(K_{mn}r)e^{X_{1C}\zeta} - \zeta e^{X_{1C}\zeta}X'_{1C}J'_m(K_{mn}r)\right]\cos(m\theta) \tag{75}$$

where

$$X'_{1C} = \frac{\partial X_{1C}}{\partial r} = \frac{\delta}{M_b}\frac{2\pi i K_{mn} r \sin\left(\tfrac{1}{2}\pi r^2\right)}{\cos^3\left(\tfrac{1}{2}\pi r^2\right)\sqrt{1 - \dfrac{4iK_{mn}\delta^2}{M_b{}^2\cos^2\left(\tfrac{1}{2}\pi r^2\right)}}} = \frac{2\pi i \delta K_{mn} r \sin\left(\tfrac{1}{2}\pi r^2\right)}{\cos^2\left(\tfrac{1}{2}\pi r^2\right)\sqrt{M_b{}^2\cos^2\left(\tfrac{1}{2}\pi r^2\right) - 4iK_{mn}\delta^2}} \tag{76}$$

Recalling that $\tilde{u}_\zeta{}^{(1)}$ must also vanish at the headwall, Eq. (75) may be integrated with respect to ζ and simplified into

$$\tilde{u}_\zeta^{(1)} = \frac{i}{K_{mn}\gamma}\frac{1}{X_{1C}}e^{-iK_m t}\left[K_{mn}^2 J_m(K_{mn}r)\left(e^{X_{1C}\zeta} - 1\right) - \frac{X'_{1C}}{X_{1C}}J'_m(K_{mn}r)\left(\zeta e^{X_{1C}\zeta}X_{1C} + 1 - e^{X_{1C}\zeta}\right)\right]\cos(m\theta) \tag{77}$$

Figure 3 showcases the unsteady velocity vectors in a chamber cross-section taken at $t = 0.01\,\text{s}$ and an axial distance of $z = 10^{-4}$ from the headwall. The four parts correspond to the same representative cases and mode numbers used to describe the acoustic pressure in Fig. 2. As one would expect, the rich vorticoacoustic wave structures that emerge are strongly influenced by the acoustic mode shapes. The nodal lines appear to be at either 90 or 45 degree angles with respect to the pressure, thus leading to horizontal (instead of vertical) symmetry in parts a) and b) where $m = 1,$ and straight crosses (instead of oblique crosses) in parts c) and d) where $m = 2.$ In comparison to the acoustic pressure distribution displayed in Fig. 2, the nodal lines of the vorticoacoustic waves are shifted by a phase angle of $\pi/(2m)$.

IV. Results and Discussion

The analytical approximations obtained heretofore can be collected into two sets of expressions for the vorticoacoustic velocity and pressure distributions. The significance of these results and the behavior of their corresponding waves will now be discussed. Furthermore, the wave behavior associated with each of the two mean flow profiles will be compared and contrasted.

To start, a summary of the vorticoacoustic wave components will be provided through the superposition of potential and rotational contributions. The resulting unsteady disturbances are given by:

Uniform injection:

$$\begin{cases} p' = e^{-iK_{mn}t} J_m\left(K_{mn}r\right)\cos\left(m\theta\right) + \mathcal{O}(M_b, \delta^2) \\ u_r' = \dfrac{i}{K_{mn}\gamma} e^{-iK_{mn}t} J_m'\left(K_{mn}r\right)\cos\left(m\theta\right)\left(1 - e^{X_1\zeta}\right) + \mathcal{O}(M_b, \delta^2) \\ u_\theta' = \dfrac{i}{K_{mn}\gamma}\dfrac{m}{r} e^{-iK_{mn}t} J_m\left(K_{mn}r\right)\sin\left(m\theta\right)\left(1 - e^{X_1\zeta}\right) + \mathcal{O}(M_b, \delta^2) \\ u_z' = \dfrac{iK_{mn}}{\gamma}\dfrac{\delta}{X_1} e^{-iK_{mn}t} J_m\left(K_{mn}r\right)\cos\left(m\theta\right)\left(e^{X_1\zeta} - 1\right) + \mathcal{O}(\delta^3) \end{cases} \tag{78}$$

Bell-shaped injection:

$$\begin{cases} p' = e^{-iK_{mn}t} J_m\left(K_{mn}r\right)\cos\left(m\theta\right) + \mathcal{O}(M_b, \delta^2) \\ u_r' = \dfrac{i}{K_{mn}\gamma} e^{-iK_{mn}t} J_m'\left(K_{mn}r\right)\cos\left(m\theta\right)\left(1 - e^{X_{1C}\zeta}\right) + \mathcal{O}(M_b, \delta^2) \\ u_\theta' = \dfrac{i}{K_{mn}\gamma}\dfrac{m}{r} e^{-iK_{mn}t} J_m\left(K_{mn}r\right)\sin\left(m\theta\right)\left(1 - e^{X_{1C}\zeta}\right) + \mathcal{O}(M_b, \delta^2) \\ u_z' = \dfrac{i}{K_{mn}\gamma}\dfrac{\delta}{X_{1C}} e^{-iK_m t}\cos\left(m\theta\right)\left[\begin{array}{l} K_{mn}^2 J_m\left(K_{mn}r\right)\left(e^{X_{1C}\zeta} - 1\right) \\ -\dfrac{X_{1C}'}{X_{1C}} J_m'\left(K_{mn}r\right)\left(\zeta e^{X_{1C}\zeta} X_{1C} + 1 - e^{X_{1C}\zeta}\right) \end{array}\right] + \mathcal{O}(\delta^3) \end{cases} \tag{79}$$

For the sake of illustration, Figs. 4, 5 and 6 are used to display the behavior of the radial, tangential and axial disturbances versus the axial coordinate at decreasing values of the inlet Mach number. This is achieved at $t = 0$, $r = 0.4$, $\theta = \frac{1}{3}\pi$, $\delta = 0.000647$ and a thrust chamber whose aspect ratio is equal to unity ($z_{\text{exit}} = L/R = 1$).[18] The corresponding plots capture the oscillatory motion for the first tangential mode using K_{10}. Furthermore, Figs 4, 5 and 6 display the unsteady velocities at two inlet Mach numbers, $M_b = 0.3$ and $M_b = 0.003$.

A. Wave Characterization

It should be noted that the expressions for unsteady radial and tangential velocities in Eqs. (78) and (79) are nearly identical. The effect of specific mean flow motion is manifested through the axial constants X_1 and X_{1C}; except for this mean flow dissimilarity, the two sets in the radial and tangential directions would have been identical. The corresponding spatial distributions are hence expected to behave similarly, with minor shifts that are caused by differences in their mean flow speeds. This observation is confirmed by the plots in Figs. 4 and 5. For example, at

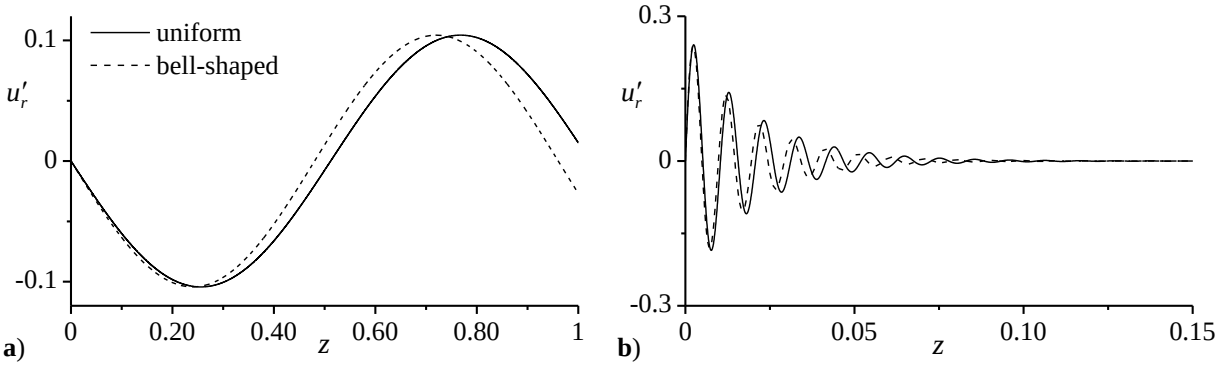

Figure 4. Unsteady radial velocity at inlet Mach numbers corresponding to: a) 0.3 and b) 0.003.

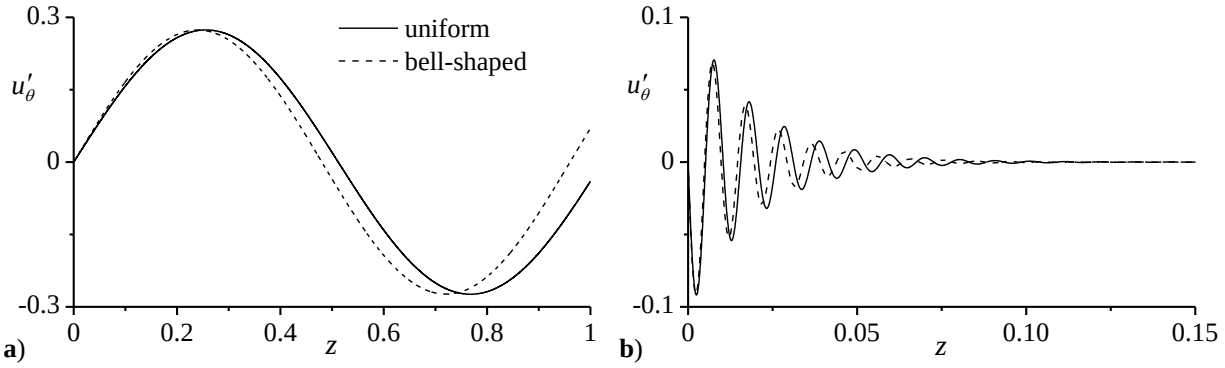

Figure 5. Unsteady tangential velocity at inlet Mach numbers corresponding to: a) 0.3 and b) 0.003.

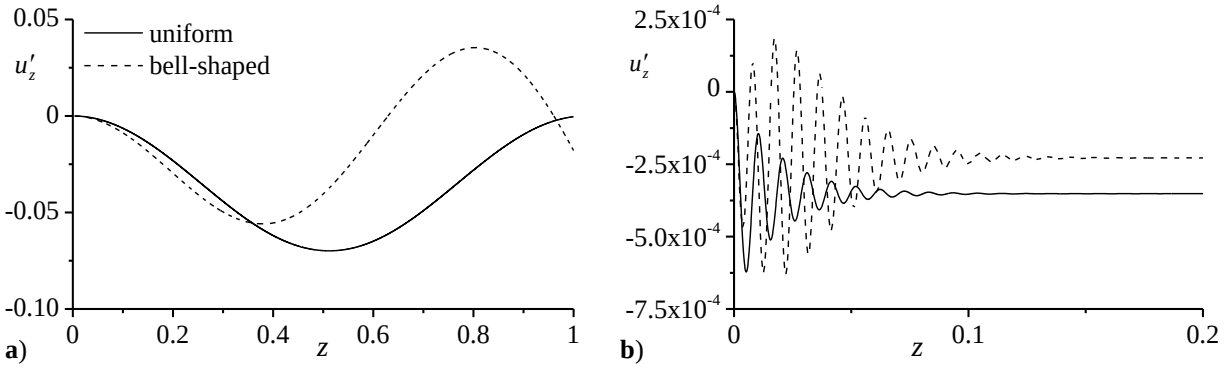

Figure 6. Unsteady axial velocity at inlet Mach numbers corresponding to: a) 0.3 and b) 0.003.

$r = 0.4$, the mean flow velocity is constant at unity for the uniform flow and 0.9686 for the bell-shaped profile. This small difference may explain the slower downstream propagation of the unsteady traveling wave associated with the bell-shaped profile relative to the solution connected with the uniform mean flow.

Interestingly, an inspection of the asymptotic orders reveals that the radial and tangential vortical velocities appear at order δ^2 (hence, of order Re_a^{-1}). This is an important observation since, in classical fluid dynamics, the normalization and subsequent analysis are traditionally based on the reciprocal of the Reynolds number, a quantity that is often taken as the primary perturbation parameter in lieu of the viscous parameter, δ. In short, it can be shown that these two velocity corrections skip every odd order and, therefore, appear only at even powers of δ. Then one may argue whether their derivation could have been achieved using the more traditional expansion, using the reciprocal of the Reynolds number. The answer is negative, owing in large part to the behavior of the axial vortical expansion. Unlike $\tilde{u}_r$ and $\tilde{u}_\theta$, the expansion of the axial vortical velocity $\tilde{u}_z$ is shifted by an order of δ from its tangential and radial counterparts, as one may infer from Eqs. (78) and (79). This may also justify the strategy used in the present approach, including the coordinate transformation that entails stretching the axial coordinate using the viscous parameter instead of the inverse of the Reynolds number.

Concerning the vortical pseudo-pressure, it may be instructive to note that, although it was not dismissed at the onset from the rotational momentum equation, it has been carefully derived and shown to be strictly zero for the first two orders in δ. We can therefore project that the vortical wave will only affect the acoustic pressure distribution starting at order δ^2. This observation confirms the analogous treatment of the longitudinal wave problem in a simulated SRM, where the vortical pressure is discarded throughout the analysis.[14,40] Here, its negligible contribution is formally demonstrated.

Returning to the wave velocity, the behavior of the vortical component in the axial direction deserves particular attention. Recalling that the acoustic component of the axial wave is discounted here (assuming a short chamber), the unsteady axial wave, u'_z, becomes confounded with the vortical part, $\tilde{u}_z$. The latter is needed to compensate for the more dominant tangential and radial components and, thus, ensure that continuity is fully satisfied. Figure 6 illustrates the behavior of u'_z for three injection Mach numbers. In these snapshots, the average unsteady velocity appears to be negative in the uniform injection case. Although the same average for the bell-shaped injection profile also proves to be negative, it exhibits a smaller absolute value. This behavior may be attributed to the speed of the

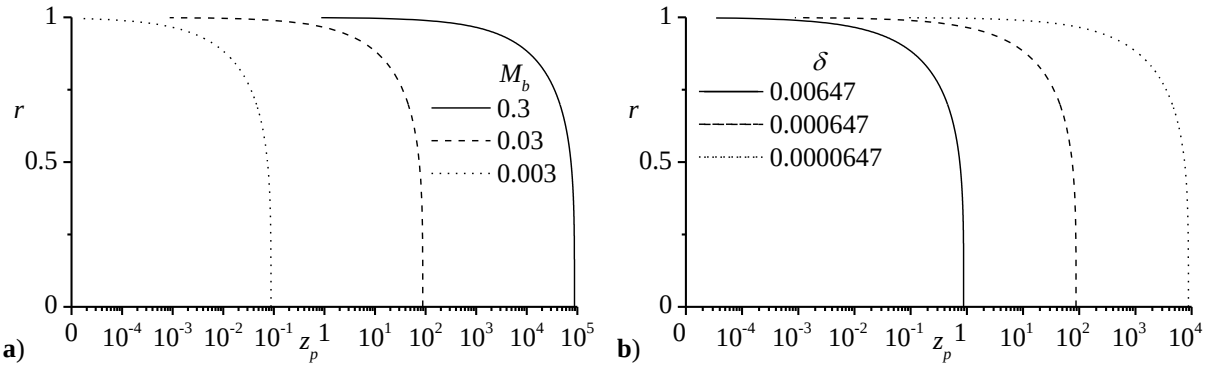

Figure 7. Different penetration depths at a) δ = 0.000647 and b) injection Mach number 0.03.

mean flow at $r = 0.4$, where the bell-shaped pattern, in comparison to the uniform motion, possesses less energy to sustain the traveling wave motion. It is thus accompanied by faster attenuation.

To further confirm this point, an inspection of the axial constant X_{1C} in Eq. (64) shows that, at the centerline, the cosine yields a value of unity that matches the uniform flow case. Moreover, as we move away toward the sidewall, the cosine function approaches zero. In close proximity of the sidewall, the axial constant tends to negative infinity, having a negative real part. It may therefore be seen that at the sidewall, Eq. (79) collapses into

$$\begin{cases} p' = e^{-iK_{mn}t} J_m\left(K_{mn} r\right)\cos\left(m\theta\right) + \mathcal{O}(M_b, \delta^2) \\ u_r' = 0 + \mathcal{O}(M_b, \delta^2) \\ u_\theta' = \dfrac{im}{K_{mn}\gamma} e^{-iK_{mn}t} J_m\left(K_{mn}\right)\sin\left(m\theta\right) + \mathcal{O}(M_b, \delta^2) \\ u_z' = 0 + \mathcal{O}(\delta^3) \end{cases} \tag{80}$$

Equation (80) shows that through the use of a bell-shaped mean flow, the ensuing transverse wave motion can intrinsically satisfy the no-slip requirement, not only at the headwall but at the sidewall as well. This is true for the dominant component of the wave, u_r' and the axial component u_z'. As for the contribution of the tangential component u_θ', its value at the sidewall is the same as that of the acoustic component, since the vortical contribution vanishes locally. It may hence be argued that the ability of this model to satisfy the physical requirements along all boundaries grants it more generality than its predecessor with uniform headwall injection.

B. Penetration Number and Rotational Layer Thickness

Figures 4, 5 and 6 illustrate the dependence of the wave's boundary layer thickness on the injection Mach number. It is apparent that the viscous forces dominate over the inertial forces as the injection Mach number is reduced. Conversely, when the injection Mach number is increased, the boundary layer is blown off the headwall.[41] It is noted that the faster decay of the wave due to the lower Mach number results in a lower propagation wavelength, measured by the peak-to-peak distance.

Physically, the behavior of the propagation wavelength may be attributed to the wave's Strouhal number, or dimensionless frequency, defined by $S = K_{mn}/M_b$. A decrement in the injection Mach number and its corresponding increment in the Strouhal number lead to a larger number of reversals per unit time. Furthermore, the increased frequency results in a higher interaction rate between fluid particles, and the increased friction between shear layers leads to a more rapid attenuation of the wave amplitude.

Mathematically, the same behavior may be deduced by rewriting the axial decay terms X_1 and X_{1C} of Eqs. (36) and (64) in terms of the Strouhal number and another dimensionless parameter. A two-term Maclaurin series approximation of X_1 and X_{1C} is required to capture the amplitude (real) and oscillatory (imaginary) components. These are

$$X_1 \approx i\frac{K_{mn}\delta}{M_b} - \frac{K_{mn}^2\delta^3}{M_b^3} = \delta\left(iS - \frac{1}{S_p}\right) \tag{81}$$

and

$$X_{1C} \approx i\frac{K_{mn}\delta}{M_b\cos\left(\frac{1}{2}\pi r^2\right)} - \frac{K_{mn}^2\delta^3}{M_b^3\cos^2\left(\frac{1}{2}\pi r^2\right)} = \delta\left[iS\sec\left(\tfrac{1}{2}\pi r^2\right) - \frac{\sec^2\left(\frac{1}{2}\pi r^2\right)}{S_p}\right] \tag{82}$$

where the effective penetration number S_p emerges in the form

$$S_p = \frac{M_b^3}{K_{mn}^2\delta^2} = \left(\frac{U_b^3}{a_0^3}\right)\left(\frac{a_0 R}{\nu_0}\right)\left(\frac{a_0^2}{\omega_0^2 R^2}\right) = \frac{U_b^3}{\nu_0\omega_0^2 R} \tag{83}$$

This parameter, first discovered by Majdalani,[42] played a key role in the characterization of the boundary layer thickness of the longitudinal vorticoacoustic wave in a simulated solid rocket motor. Note that an increase in S_p leads to a deeper penetration of the wave. From a physical standpoint, the penetration number gauges the balance between two basic forces: unsteady inertia and viscous diffusion of the radial and tangential velocities in the axial direction. For the radial velocity, S_p may be viewed as the ratio of

$$\frac{\text{unsteady inertial force}}{\text{viscous force}} \approx \frac{\dfrac{\partial u_r^*}{\partial t^*}}{\nu\dfrac{\partial^2 u_r^*}{\partial z^{*2}}} \approx \frac{\dfrac{u_r^*}{t^*}}{\nu\dfrac{u_r^*}{z^{*2}}} = \frac{z^{*2}}{\nu t^*} \approx \frac{(U_b/\omega_0)^2}{\nu(R/U_b)} = \frac{U_b^3}{\nu_0\omega_0^2 R} = S_p \tag{84}$$

In the present study, the wave expressions can be recast using the Strouhal and penetration numbers. For the bell-shaped injection profile, the (real) magnitudes of the waves in Eq. (79) are seen to be governed by

$$u_r' \sim J_m'\left(K_{mn}r\right)\left[1-\exp\left(-\frac{z}{S_p\cos^2\eta}\right)\right] \tag{85}$$

$$u_\theta' \sim J_m\left(K_{mn}r\right)\left[1-\exp\left(-\frac{z}{S_p\cos^2\eta}\right)\right] \tag{86}$$

and

$$u_z' \sim S_p\cos\eta\left\{\begin{array}{l} K_{mn}^2 J_m\left(K_{mn}r\right)\left[\exp\left(-\dfrac{z}{S_p\cos^2\eta}\right)-1\right] \\ -\pi r\tan\eta J_m'\left(K_{mn}r\right)\left[\dfrac{z}{S_p\cos^2\eta}\exp\left(-\dfrac{z}{S_p\cos^2\eta}\right)-\exp\left(-\dfrac{z}{S_p\cos^2\eta}\right)+1\right] \end{array}\right\} \tag{87}$$

where $\eta \equiv \frac{1}{2}\pi r^2$.

A simple inspection of Eqs. (85)–(87) reveals that, at the sidewall, the radial and axial components vanish, while the tangential component scales with $J_m\left(K_{mn}\right)$; this behavior is consistent with the observations of the previous section. The rotational boundary layer can also be deduced from Eqs. (85) and (86). The penetration of rotational elements is traditionally defined as the distance from the injecting boundary to the point where the contribution of the vortical wave becomes negligible, traditionally taken at 1% of the acoustic wave.[41] Since the axial component of the potential field vanishes in the farfield, the penetration depth may be deduced for the radial and tangential components by taking:

$$\exp\left(-\frac{z}{S_p\cos^2\eta}\right) = \alpha = 0.01 \tag{88}$$

where α corresponds to 1% and z_p denotes the axial thickness of the rotational boundary layer. Rearranging Eq. (88) renders

$$z_p = S_p\cos^2\left(\tfrac{1}{2}\pi r^2\right)\ln(\alpha^{-1}) = \frac{M_b^3}{K_{mn}^2\delta^2}\cos^2\left(\tfrac{1}{2}\pi r^2\right)\ln(\alpha^{-1}) \tag{89}$$

Figure 7 correlates the thickness of the vorticoacoustic boundary layer to the injection Mach number and viscous parameter. In conjunction with the expression in Eq. (89), Fig. 7 shows that the boundary layer is thick for large injection Mach numbers, exceeding by far the length of the chamber. When this case occurs, the linear oscillations have no time to decay before exiting the chamber, which would be entirely subject to transverse waves. On the other hand, in the case of a small injection Mach number, the oscillations would take their toll almost entirely in the injector zone before fading out elsewhere. A balance between both is required to deduce the effect of the wave on

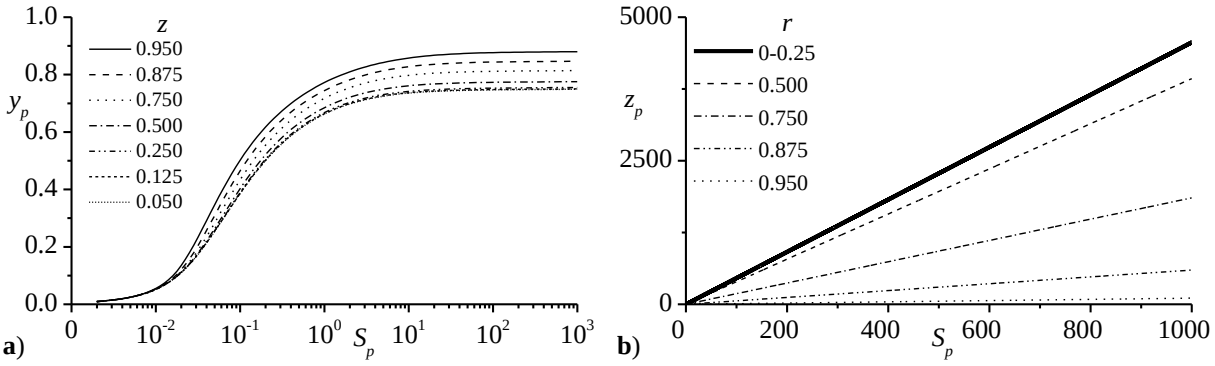

Figure 8. Penetration depth of the vortical wave corresponding to a) axial[41] and b) transverse configurations.

the chamber. Moreover, the dependence on the injection pattern is apparent in the expression of the penetration depth. The boundary layer thickness reaches its peak at the centerline, where disturbances are convected into the chamber at the largest headwall velocity and then depreciates precipitously to zero at the sidewall where the mean flow is forced to rest.

Figure 8 compares the dependence of the boundary layer's thickness on the penetration number in the axial (SRM) and transverse (LRE) cases. The effects of the different injection mechanisms are reflected in these plots. In a solid rocket motor, particles injected radially at the sidewall must turn before merging in the longitudinal direction parallel to the chamber axis. This causes the penetration depth to increase in the direction along which unsteady vorticity is convected by virtue of the mean flow. Conversely, in the liquid rocket engine, injection takes place at the headwall and remains unaffected by the downstream convection of unsteady vorticity. The thickness of the boundary layer is thus dependent only on the speed of injection. Throughout the chamber, a linear correlation, given by Eq. (89), prescribes the depth of penetration. Unlike the axially dominated wave problem for which the wall-normal depth of penetration y_p approaches a maximum inviscid upper limit as $S_p \to \infty$, the axial depth of penetration, z_p, will continue to grow linearly with S_p up to the point where the injection M_b would have exceeded the physical limitations of the model.

C. Wave Properties

In addition to the penetration depth, three properties must be investigated to complete our characterization of the vorticoacoustic wave behavior. These consist of the spatial wavelength, λ, the unsteady velocity overshoot factor, OF, and its spatial locus, z_{OS}. Since the radial and tangential components have similar expressions, the following analysis is performed using the radial component only. Nonetheless, the upcoming procedure is applicable to both waves.

1. Spatial Wavelength

The spatial wavelength, λ, defines the distance traveled by a wave during one period. It is also referred to as the distance between two consecutive peaks. To calculate λ, the wave propagation speed in the axial direction must be determined. The radial component of the vortical wave in Eq. (79) can be rewritten as

$$\tilde{u}_r = F(r,\theta,z)\exp\left\{i\left[S\sec\left(\tfrac{1}{2}\pi r^2\right)z - K_{mn}t\right]\right\} \tag{90}$$

where F represents the amplitude of the wave. With the propagation of the wave in the axial direction being our primary concern, differentiation of the axial component is required to find the corresponding velocity. We have

$$S\sec\left(\tfrac{1}{2}\pi r^2\right)\mathrm{d}z - K_{mn}\mathrm{d}t = 0 \quad \text{or} \quad V_w = \frac{\mathrm{d}z}{\mathrm{d}t} = \frac{K_{mn}\cos\left(\tfrac{1}{2}\pi r^2\right)}{S} = M_b\cos\left(\tfrac{1}{2}\pi r^2\right) \tag{91}$$

Knowing that the period of oscillation is $\tau = 2\pi/K_{mn}$, the spatial wavelength is retrieved as

$$\lambda_s = V_w\tau = \frac{\cos\left(\tfrac{1}{2}\pi r^2\right)}{S} \tag{92}$$

Consistent with classic theory of periodic flows, we note that the velocity of propagation is dependent only on the medium and conditions, i.e. the injection Mach number and the radial distance from the centerline. Moreover, the wavelength depends on the mode number, which is embedded in the Strouhal number. Higher modes reduce the

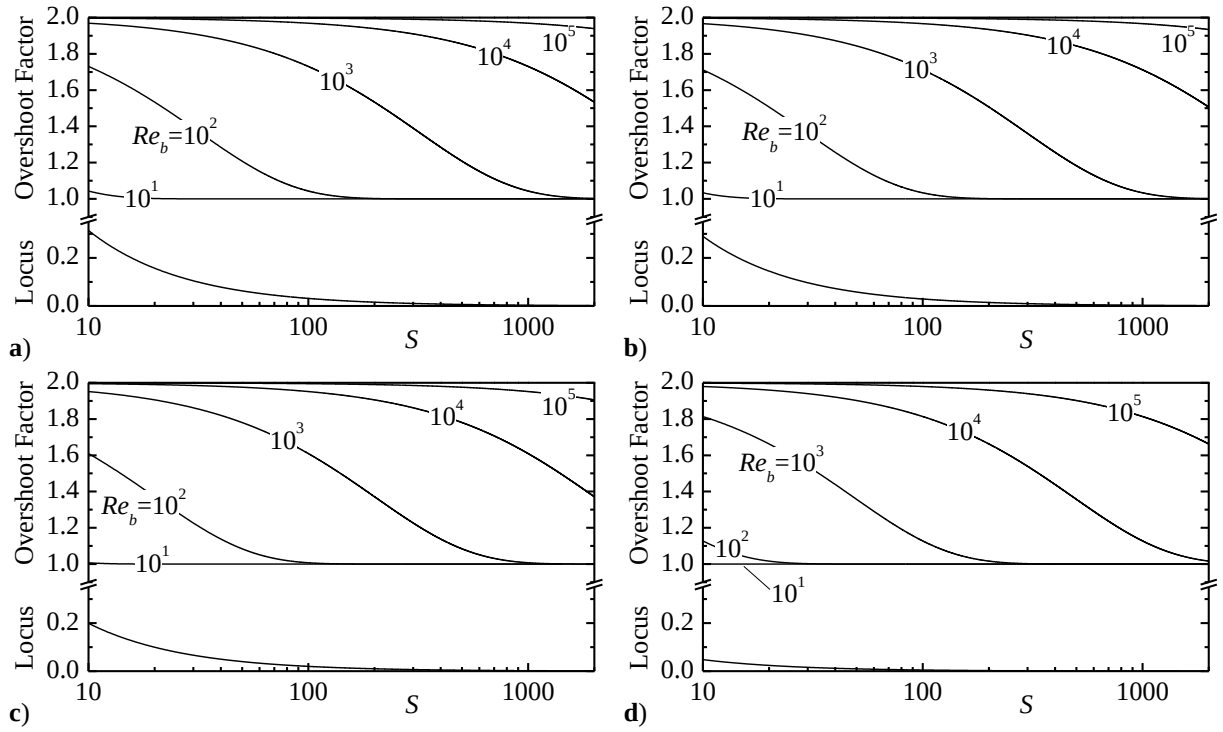

Figure 9. Overshoot factor and locus of overshoot at a) $r = 0$, b) $r = 0.5$, c) $r = 0.75$ and d) $r = 0.95$.

peak-to-peak distance between oscillations, as one would expect. An important characteristic of this model is the dependence of all properties on the radial distance from the centerline. Accordingly, oscillations in the vicinity of the sidewall propagate at a much slower rate than those located near the chamber core.

2. Unsteady Velocity Overshoot

The presence of the Strouhal number argument in the vortical solution controls the phase difference between the strictly acoustic and vortical waves. Due to their phase difference, the two waves will periodically couple at nearly the same phase, thus resulting in an overshoot of the unsteady velocity that can reach, in some cases, twice the acoustic wave amplitude. This overshoot was first discovered by Richardson[43] who realized that maximum velocities in reciprocating flows occurred in the vicinity of the sidewall, rather than the centerline of his resonator tubes. The overshoot was later dubbed 'Richardson's annular effect.'

Knowing that the overshoot takes place when both waves travel in phase, this condition corresponds to $\tilde{u}_r = -F(r,\theta,z)\exp(-iK_{mn}t)$, according to Eq. (90); the locus of the overshoot can thus be deduced to be

$$z_{\mathrm{OS}} = \frac{\pi}{S}\cos\left(\tfrac{1}{2}\pi r^2\right) \tag{93}$$

Since the problem and its corresponding solution are normalized, the induced overshoot factor can be determined by combining the axial contribution of the vortical correction to that of the acoustic wave. The overshoot factor OF can be extracted from Eq. (79) and (82) by evaluating the amplitude of the vorticoacoustic velocity at $z = z_{\mathrm{OS}}$. Starting with

$$\mathrm{OF} = 1 - \exp\left[iS\sec\left(\tfrac{1}{2}\pi r^2\right) z_{\mathrm{OS}} - \frac{\sec^2\left(\tfrac{1}{2}\pi r^2\right)}{S_p} z_{\mathrm{OS}} \right] \tag{94}$$

$$\mathrm{OF} = 1 - \exp\left[i\pi - \frac{\pi}{\cos\left(\tfrac{1}{2}\pi r^2\right)} \frac{1}{SS_p} \right] = 1 + \exp\left[-\frac{\pi}{\cos\left(\tfrac{1}{2}\pi r^2\right)} \frac{1}{SS_p} \right] \tag{95}$$

or

$$\mathrm{OF} = 1 + \exp\left[-\frac{\pi S}{\cos\left(\tfrac{1}{2}\pi r^2\right)} \frac{\delta^2}{M_b} \right] = 1 + \exp\left[-\frac{\pi}{\cos\left(\tfrac{1}{2}\pi r^2\right)} \frac{S}{Re_b} \right] \tag{96}$$

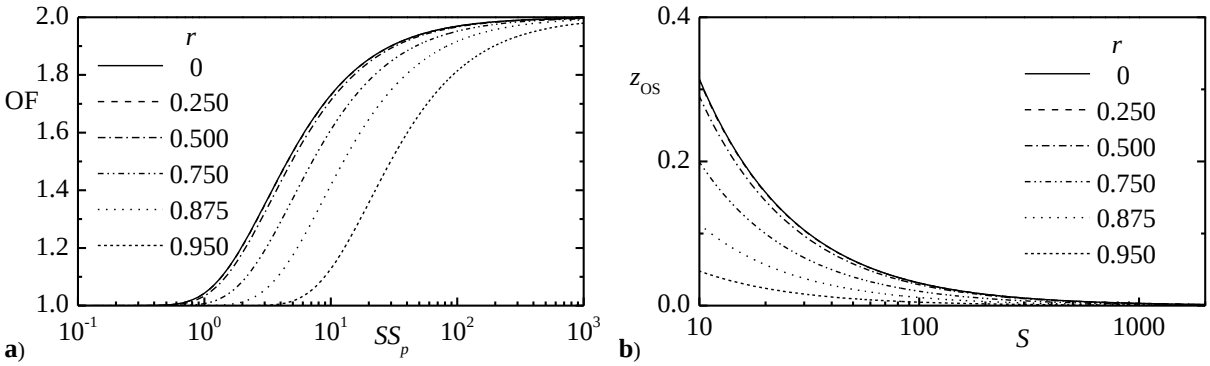

Figure 10. Effect of radial distance on a) the wave overshoot factor and b) its locus.

Figure 9 quantifies the overshoot factor and its locus for different control parameters. Note that on one hand, OF depends on the Strouhal number, the distance from the centerline and the average chamber viscosity; the latter is accounted for through the blowing Reynolds number at the headwall, $Re_b = M_b Re_a = U_b R/\nu_0$. On the other hand, the different figures and their families of curves dramatically collapse into single lines (shown in Fig. 10a) when plotted versus the product of the Strouhal and penetration numbers. Figure 10a shows that the strength of the overshoot decreases as we move away from the chamber centerline and increases at higher values of SS_p, i.e. with larger injection velocities or smaller frequencies. However, the locus of the overshoot depends solely on the Strouhal number and the distance from the centerline. For all physical values of the Strouhal number, the overshoot takes place in a region smaller than 25 percent of the chamber radius in the neighborhood of the headwall. Recalling that faceplate injectors protrude inwardly, they can be subject to oscillations reaching twice the strength of the predicted acoustic waves, even in the linear range. Additionally, it appears that the distance from the centerline affects the overshoot and its properties. The slower injection rate near the sidewalls leads to a smaller overshoot factor. Furthermore, as one may infer from Eq. (93) and Fig. 10b, z_{OS} decreases while moving away from the centerline to the extent of vanishing along the sidewall. This behavior shifts the line of maximum wave amplitude closer to the headwall as the sidewall is approached. In the case of a liquid rocket engine, these spatial excursions of peak transverse amplitudes serve to amplify shearing stresses on the injectors, where coupling between modes can lead to further steepening and shock-like behavior.

V. Conclusions

In this study, asymptotic expansion tools are used to capture small-to-moderate amplitude oscillations that are dominated by their transverse motion in a short circular cylinder that mimics the cold flow environment of a simple liquid rocket engine. Two particular formulations are advanced, and these correspond to either uniform or bell-shaped cosine-like injection at the chamber headwall. After decomposing the unsteady wave into potential and rotational fields, the latter is resolved using a boundary layer formulation that relies on a small viscous parameter, δ. This parameter corresponds to the square root of the inverted Reynolds number based on viscosity and the speed of sound. At the outset, several fundamental flow features are unraveled including the radial, tangential, and axial velocities of the time-dependent vortical field. The pseudo-pressure associated with the rotational motion is also determined rigorously and shown to be immaterial to the present analysis. The penetration number, a keystone parameter that controls the so-called depth of penetration of unsteady vorticity, is also identified. It is found to be nearly identical to its counterpart arising in the longitudinal wave analog encountered in the treatment of oscillatory motion in solid rocket motors.[14,40] The advent of this parameter enables us to fully characterize the depth of penetration in the direction normal to the injecting surface. Furthermore, our formulation for the unsteady motion connected with uniform headwall injection is found to be consistent with a previous study aimed at investigating acoustic streaming effects in a similar geometric setting.[18] The zeroth-order injection model, however, leads to a transverse wave solution that allows slip along the sidewall. An improved formulation is herein produced based on a bell-shaped injection profile that gives rise to a more suitable representation of the oscillatory field. The latter is shown to satisfy the no-slip boundary at both headwall and chamber sidewall for the radial and axial components. It is hoped that the mathematical strategy presented here can be later used to target higher order models of three-dimensional traveling and standing waves in various geometric settings.

With the vorticoacoustic solution at hand, fundamental wave propagation properties are carefully extracted and discussed. These include the depth of penetration and Richardson's overshoot factor of the transverse waves. These are found to be strongly dependent on the Strouhal and penetration numbers; the latter represents a keystone parameter that seems to recur whenever oscillatory wave motion is considered above an injecting surface. The locus of peak wave amplitude, in particular, is found to be smaller than a quarter radius, thus placing the maximum shearing stresses resulting from transverse wave motion in the close vicinity of the headwall. In future work, the steepening of these waves will be examined.

Acknowledgments

This material is based on work supported partly by the National Science Foundation through Grant No. CMMI-0928762, and partly by the University of Tennessee Space Institute, through institutional cost sharing.

References

[1]Richecoeur, F., Ducruix, S., Scouflaire, P., and Candel, S., "Experimental Investigation of High-Frequency Combustion Instabilities in Liquid Rocket Engine," *Acta Astronautica,* Vol. 62, No. 1, 2008, pp. 18-27. doi: 10.1016/j.actaastro.2006.12.034

[2]Smith, R., Ellis, M., Xia, G., Sankaran, V., Anderson, W., and Merkle, C. L., "Computational Investigation of Acoustics and Instabilities in a Longitudinal-Mode Rocket Combustor," *AIAA Journal,* Vol. 46, No. 11, 2008, pp. 2659-2673. doi: 10.2514/1.28125

[3]Fischbach, S. R., and Majdalani, J., "Volume-to-Surface Reduction of Vorticoacoustic Stability Integrals," *Journal of Sound and Vibration,* Vol. 321, No. 3-5, 2009, pp. 1007-1025. doi: 10.1016/j.jsv.2008.10.001

[4]Flandro, G. A., Majdalani, J., and Sims, J. D., "Nonlinear Longitudinal Mode Instability in Liquid Propellant Rocket Engine Preburners," AIAA Paper 2004-4162, July 2004.

[5]Flandro, G. A., Majdalani, J., and Sims, J. D., "On Nonlinear Combustion Instability in Liquid Propellant Rocket Engines," AIAA Paper 2004-3516, July 2004.

[6]Clayton, R. M., "Experimental Measurements on Rotating Detonation-Like Combustion," Jet Propulsion Laboratory, Technical Report 32-788, Pasadena, CA, August 1965.

[7]Clayton, R. M., Rogero, R. S., and Sotter, J. G., "An Experimental Description of Destructive Liquid Rocket Resonant Combustion," *AIAA Journal,* Vol. 6, No. 7, 1968, pp. 1252-1259.

[8]Sotter, J. G., Woodward, J. W., and Clayton, R. M., "Injector Response to Strong High-Frequency Pressure Oscillations," *Journal of Spacecraft and Rockets,* Vol. 6, No. 4, 1969, pp. 504-506. doi: 10.2514/3.29696

[9]Ando, D., Inaba, K., and Yamamoto, M., "Numerical Investigation on the Transverse Wave Property of Two-Dimensional H_2-O_2-Diluent Detonations," AIAA Paper 2007-5655, January 2007.

[10]Chandrasekhar, S., and Chakravarthy, S., "Response of Non-Premixed Ducted Flame to Transverse Oscillations and Longitudinal Acoustic Coupling," AIAA Paper 2007-989, July 2007.

[11]Hart, R. W., and McClure, F. T., "Combustion Instability: Acoustic Interaction with a Burning Propellant Surface," *The Journal of Chemical Physics,* Vol. 30, No. 6, 1959, pp. 1501-1514. doi: 10.1063/1.1730226

[12]Hart, R. W., and McClure, F. T., "Theory of Acoustic Instability in Solid-Propellant Rocket Combustion," *Tenth Symposium (International) on Combustion,* Vol. 10, No. 1, 1965, pp. 1047-1065.

[13]Culick, F. E. C., "Acoustic Oscillations in Solid Propellant Rocket Chambers," *Acta Astronautica,* Vol. 12, No. 2, 1966, pp. 113-126.

[14]Majdalani, J., and Roh, T. S., "The Oscillatory Channel Flow with Large Wall Injection," *Proceedings of the Royal Society of London, Series A,* Vol. 456, No. 1999, 2000, pp. 1625-1657. doi: 10.1098/rspa.2000.0579

[15]Fabignon, Y., Dupays, J., Avalon, G., Vuillot, F., Lupoglazoff, N., Casalis, G., and Prévost, M., "Instabilities and Pressure Oscillations in Solid Rocket Motors," *Journal of Aerospace Science and Technology,* Vol. 7, No. 3, 2003, pp. 191-200. doi: 10.1016/S1270-9638(02)01194-X

[16]Culick, F. E. C., "High Frequency Oscillations in Liquid Rockets," *AIAA Journal,* Vol. 1, No. 5, 1963, pp. 1097-1104.

[17]Fischbach, S. R., Majdalani, J., and Flandro, G. A., "Acoustic Instability of the Slab Rocket Motor," *Journal of Propulsion and Power,* Vol. 23, No. 1, 2007, pp. 146-157.

[18]Fischbach, S., Flandro, G., and Majdalani, J., "Acoustic Streaming in Simplified Liquid Rocket Engines with Transverse Mode Oscillations," *Physics of Fluids,* Vol. 22, No. 6, 2010, pp. 063602-21. doi: 10.1063/1.3407663

[19]Maslen, S. H., and Moore, F. K., "On Strong Transverse Waves without Shocks in a Circular Cylinder," *Journal of the Aeronautical Sciences,* Vol. 23, 1956, pp. 583-593.

[20]Crocco, L., Harrje, D., and Reardon, F., "Transverse Combustion Instability in Liquid Propellant Rocket Motors," *Journal American Rocket Society,* Vol. 32, 1962, p. 366.

[21]Culick, F. E. C., "Rotational Axisymmetric Mean Flow and Damping of Acoustic Waves in a Solid Propellant Rocket," *AIAA Journal,* Vol. 4, No. 8, 1966, pp. 1462-1464. doi: 10.2514/3.3709

[22]Brown, R. S., Blackner, A. M., Willoughby, P. G., and Dunlap, R., "Coupling between Acoustic Velocity Oscillations and Solid Propellant Combustion," *Journal of Propulsion and Power,* Vol. 2, No. 5, 1986, pp. 428-437. doi: 10.2514/3.22925

[23]Dunlap, R., Blackner, A. M., Waugh, R. C., Brown, R. S., and Willoughby, P. G., "Internal Flow Field Studies in a Simulated Cylindrical Port Rocket Chamber," *Journal of Propulsion and Power,* Vol. 6, No. 6, 1990, pp. 690-704. doi: 10.2514/3.23274

[24]Vuillot, F., and Avalon, G., "Acoustic Boundary Layer in Large Solid Propellant Rocket Motors Using Navier-Stokes Equations," *Journal of Propulsion and Power,* Vol. 7, No. 2, 1991, pp. 231-239. doi: 10.2514/3.23316

[25]Majdalani, J., and Van Moorhem, W. K., "A Multiple-Scales Solution to the Acoustic Boundary Layer in Solid Rocket Motors," *Journal of Propulsion and Power,* Vol. 13, No. 2, 1997, pp. 186-193. doi: 10.2514/2.5168

[26]Majdalani, J., and Van Moorhem, W. K., "Improved Time-Dependent Flowfield Solution for Solid Rocket Motors," *AIAA Journal,* Vol. 36, No. 2, 1998, pp. 241-248. doi: 10.2514/2.7507

[27]Majdalani, J., and Flandro, G. A., "The Oscillatory Pipe Flow with Arbitrary Wall Injection," *Proceedings of the Royal Society of London, Series A,* Vol. 458, No. 2023, 2002, pp. 1621-1651. doi: 10.1098/rspa.2001.0930

[28]Berman, A. S., "Laminar Flow in Channels with Porous Walls," *Journal of Applied Physics,* Vol. 24, No. 9, 1953, pp. 1232-1235. doi: 10.1063/1.1721476

[29]Yuan, S. W., and Finkelstein, A. B., "Laminar Pipe Flow with Injection and Suction through a Porous Wall," *Transactions of the American Society of Mechanical Engineers: Journal of Applied Mechanics,* Vol. 78, No. 3, 1956, pp. 719-724.

[30]Zinn, B. T., and Savell, C. T., "A Theoretical Study of Three-Dimensional Combustion Instability in Liquid-Propellant Rocket Engines," *Symposium (International) on Combustion,* Vol. 12, No. 1, 1969, pp. 139-147. doi: 10.1016/s0082-0784(69)80398-x

[31]Chu, B.-T., and Kovásznay, L. S. G., "Non-Linear Interactions in a Viscous Heat-Conducting Compressible Gas," *Journal of Fluid Mechanics,* Vol. 3, No. 5, 1958, pp. 494-514. doi: 10.1017/S0022112058000148

[32]Sutton, G. P., and Biblarz, O., *Rocket Propulsion Elements,* John Wiley, New York, 2001.

[33]Proudman, I., "An Example of Steady Laminar Flow at Large Reynolds Number," *Journal of Fluid Mechanics,* Vol. 9, No. 4, 1960, pp. 593-602. doi: 10.1017/S002211206000133X

[34]Beddini, R. A., "Injection-Induced Flows in Porous-Walled Ducts," *AIAA Journal,* Vol. 24, No. 11, 1986, pp. 1766-1773. doi: 10.2514/3.9522

[35]Chedevergne, F., Casalis, G., and Féraille, T., "Biglobal Linear Stability Analysis of the Flow Induced by Wall Injection," *Physics of Fluids,* Vol. 18, No. 1, 2006, pp. 014103-14. doi: 10.1063/1.2160524

[36]Griffond, J., and Casalis, G., "On the Nonparallel Stability of the Injection Induced Two-Dimensional Taylor Flow," *Physics of Fluids,* Vol. 13, No. 6, 2001, pp. 1635-1644. doi:10.1063/1.1367869

[37]Majdalani, J., and Saad, T., "The Taylor-Culick Profile with Arbitrary Headwall Injection," *Physics of Fluids,* Vol. 19, No. 9, 2007, pp. 093601-10. doi: 10.1063/1.2746003

[38]Majdalani, J., "Analytical Models for Hybrid Rockets," *Fundamentals of Hybrid Rocket Combustion and Propulsion,* edited by K. Kuo and M. J. Chiaverini, AIAA Progress in Astronautics and Aeronautics, Washington, DC, 2007, pp. 207-246.

[39]Carrier, B. T., and Carlson, F. D., "On the Propagation of Small Disturbances in a Moving Compressible Fluid," *Quarterly of Applied Mathematics,* Vol. 4, No. 1, 1946, pp. 1-12.

[40]Majdalani, J., "Multiple Asymptotic Solutions for Axially Travelling Waves in Porous Channels," *Journal of Fluid Mechanics,* Vol. 636, No. 1, 2009, pp. 59-89. doi: 10.1017/S0022112009007939

[41]Majdalani, J., "The Boundary Layer Structure in Cylindrical Rocket Motors," *AIAA Journal,* Vol. 37, No. 4, 1999, pp. 505-508. doi: 10.2514/2.742

[42]Majdalani, J., "Improved Flowfield Models in Rocket Motors and the Stokes Layer with Sidewall Injection," Ph.D. Dissertation, University of Utah, 1995.

[43]Richardson, E. G., "The Amplitude of Sound Waves in Resonators," *Proceedings of the Physical Society, London,* Vol. 40, No. 27, 1928, pp. 206-220.